International Journal of
Turbomachinery
Propulsion and Power

MDPI

Article

Optimizing Functionality of Pressurized Sewerage Systems †

Tobias Rinnert *, Tim Nitzsche, David Beck, Florian Brokhausen and Paul Uwe Thamsen

Department of Fluid System Dynamics, Technische Universität Berlin, 10623 Berlin, Germany; tim.nitzsche@tu-berlin.de (T.N.); david.beck@tu-berlin.de (D.B.); florian.brokhausen@tu-berlin.de (F.B.); paul-uwe.thamsen@tu-berlin.de (P.U.T.)

* Correspondence: t.rinnert@tu-berlin.de; Tel.: +49-(0)30-314-70930

† This paper presents a consolidated and extended version of the papers published in the proceedings of the Conference on Modelling Fluid Flow (CMFF'25) in Budapest, Hungary, 26–29 August 2025.

Abstract

This paper presents methods and results on optimizing the functionality of pressurized sewerage systems, specifically wastewater pumping stations. A holistic approach is introduced to address major issues in wastewater transport such as sedimentation in suction chambers and fiber-induced issues in wastewater pumps, as well as their effects and detection. A conceptual suction chamber is scaled using hydraulic similarity and is experimentally investigated regarding its susceptibility to sedimentation. Optimization of inlets and manifolds, pumps, and sloped walls contribute to minimizing sedimentation. In terms of wastewater pumps, a semi-open two-channel wastewater impeller is optimized for its efficiency via response surface optimization. The subsequent optimization for functionality showcases the nexus of the two characteristics by means of cut-back and thickened leading edges, which significantly reduce the susceptibility to clogging. Another important consideration in wastewater pump design is the back shroud cavity. Through iterative experiments with different housing recess configurations, the back shroud cavity is optimized to minimize fiber entry and protect the mechanical seal. Lastly, the demonstration of the effects of clogging in the form of transient instationarities in the torque of a wastewater pump underline the importance of optimizing wastewater pumps for their functionality and low susceptibility to clogging.

Keywords: back shroud cavity; clogging; frequency-domain analysis; housing recess; instationary mechanical load; optimization; physical model; pumping station; sedimentation; wastewater pump

Check for updates

Academic Editors: János Gábor Vad, Csaba Horváth and Esztella Éva Balla

Received: 28 February 2026
Revised: 12 July 2026
Accepted: 28 July 2026
Published: 1 September 2026

Copyright: © 2026 by the authors. Published by MDPI on behalf of the European Turbomachinery Society. Licensee MDPI, Basel, Switzerland. This article is an open access article distributed under the terms and conditions of the Creative Commons Attribution (CC BY-NC-ND) license.

1. Introduction

Within pressurized sewerage systems, wastewater pumping stations are essential to transporting wastewater from the incoming free-flow sewer to the treatment plant via pressure pipes. However, due to the high proportion of solids and the general heterogeneous nature of wastewater [1,2], a variety of challenges such as sedimentation, swimming layers, fiber-induced pump clogging [3] and air entrainment [4] occur in pumping stations. In order to ensure trouble-free and low-maintenance operation of the entire pumping station, it is necessary to take all key components into holistic consideration.

In terms of suction chamber design considerations, these include pit shape, inlet layout and the geometry of the sloped walls, among other things. To optimize and validate these parameters, an investigation using hydraulic models is recommended [5,6]. These are leveraged to ensure the transportation of solids and avoid sedimentation in the suction

chamber design. However, the benefits of such optimizations are limited if the downstream pump cannot handle the transportation of the amounts of solids within the wastewater. Generally, requirements on wastewater pumps, such as clogging-free, safe and efficient operation [7,8] are increasingly challenging to meet, as amounts of solids and fibers in particular have increased in wastewater. The fibers contained in wastewater frequently accumulate in wastewater pumps at the blade inlet, on the cutwater and in the front and back shroud cavity [7,9,10]. This can result in obstructions that can impair pump performance and, in extreme cases, lead to complete system failure [11].

In order to meet the requirements discussed, there are numerous design guidelines available that vary depending on wastewater composition [12,13]. Wastewater pumps are thus usually designed as single-stage pumps with a volute or annular casing [7,9]. This is due to the fact that the bladed guide vanes found in multistage pumps are prone to clogging [9,12]. Furthermore, balance holes in the back shroud are avoided in wastewater pumps as well for the same reason, so that axial thrust reduction is typically achieved by back vanes [9]. In wastewater pumps, vortex as well as one-, two- and three-channel impellers are commonly employed [7]. When pumping large solids, clogging can be easily avoided by choosing wastewater impellers that feature a sufficiently large *ball passage* [9]. When it comes to pumping fiber-laden wastewater, however, susceptibility to clogging is independent of the ball passage, as experimentally determined by Pöhler and Thamsen [14] for a wide variety of wastewater pump impellers. Further experiments show that neither the impeller type nor the performance class have an influence on *functionality* [15], i.e., the ability of a pump to transport fiber-laden wastewater without clogging [5]. Overall efficiency is also not correlated with functionality [15]. Moreover, it is shown in [16,17] that geometric modifications of a wastewater impeller can significantly increase the functionality of wastewater pumps. The optimal designs investigated in these works demonstrate the nexus of functionality and efficiency in wastewater pumps, deducing the mutual exclusivity of either optimum.

In addition to the risk of clogging, fibers entering the back shroud cavity can pose a risk to the mechanical seal [18]. However, only vague design guidelines are available to keep the back shroud cavity free of fibers or other solids. Housing recesses as well as back vanes are stated as possible solutions [9,18–20]. In preliminary analyses, fiber entry into the back shroud cavity is found to significantly decrease as the axial gap width between flat-disk-shaped back shroud and rear housing wall decreases [21]. Further investigations focus on the influence of specific design parameters for backward curved back vanes on fiber entry into the back shroud cavity [22]. It is shown that backward curved back vanes can eliminate fiber entry into the back shroud completely even at low back vane height and with minor efficiency drawbacks.

Any measures to increase the functionality of wastewater pumps can never guarantee clogging-free operation but decrease susceptibility to clogging. The heterogeneous and unpredictable properties of wastewater can vary within a very short time, making the monitoring of the operational behavior paramount. Therefore, the undesired consequences of clogging, such as reductions in flow rate or pump head, increased energy consumption, and amplified mechanical stress and wear, need to be identified, characterized, and can be leveraged in the identification of critical operational behavior. The characterization of clogging-induced effects on torque in the form of transient instationarities is investigated and demonstrated to coincide with the susceptibility to clogging of a pump.

The focus of this paper is to show how the holistic optimization of suction chamber and pump design using experimental and numerical methods together with the characterization of clogging-induced operational instationarities can contribute to the trouble-free, safe, and cost-effective operation of pumping stations. To this end, optimizations are made to the

suction chamber geometry, the pump impeller geometry, and the housing recess geometry in the back shroud cavity.

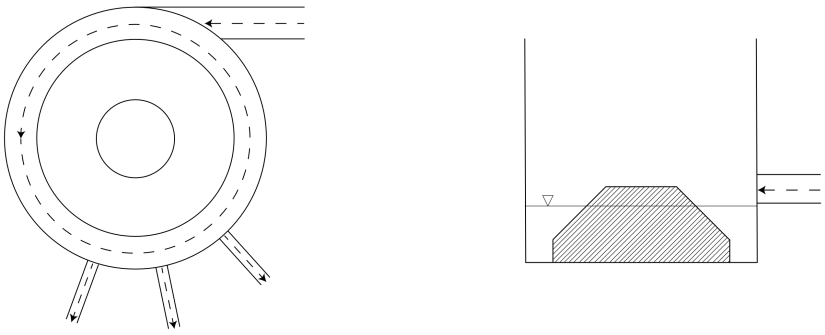
The chair of Fluid System Dynamics at Technische Universität Berlin conducts extensive research on the optimization of suction chambers [23] and wastewater pumps [16,17,21,22,24,25], as well as the characterization of clogging-induced phenomena [26–28] and their detection [29,30]. The methods and results presented in this paper offer a comprehensive overview of current research efforts in these areas.

2. Minimizing Sedimentation in Round Wastewater Pumping Stations

2.1. Background

Wastewater transport using pressure pipes can be realized by upstream wastewater pumping stations. These structures can vary greatly in size and design. In principle, they can be classified according to the pumps used. Dry-installed pumps are housed in separate machine rooms. While this allows for easier maintenance and inspection of the machines, it requires increased constructional investment. Wet-installed pumps are placed directly in the suction chamber [7].

The pumping station described in this paper is a variant with dry-installed pumps. The relevant standards contain recommendations for these systems for pumps positioned next to each other. This constellation often results in a suction chamber which is rectangular in shape and provides increased opportunities for particle deposits around the edges. In order to achieve higher flow velocity and thus better activation of particles, a circular suction chamber with dry-installed pumps was developed as the initial concept. A central cone was used to increase particle movement and prevent the formation of a swimming layer in the outer channel. A schematic top view of the pump station is shown in Figure 1a. A schematic sectional view is shown in Figure 1b. Dashed arrows symbolize the wastewater flow in both illustrations from inlet to the pumps. The left and middle outlets represent the two rainwater pumps, and the right pipe shows the position of the dry-weather pump. The distance from the inlet of the suction pipes to the bottom of the tank is $D/2$. For all three pumps, the diameter of the suction pipe inlets D is 0.082 m.



(**a**) top view (**b**) sectional view

Figure 1. Concept of round suction chamber with central cone.

The connection to the wastewater network takes place in two stages over several years, during which the number of inhabitants covered increases. In order to cover the two operating requirements, both expansion stage 1 with a lower incoming flow rate and expansion stage 2 with increased flow are taken into consideration in the following investigations.

2.2. Materials and Methods

2.2.1. Dimensioning

In order to carry out a fluidic analysis using a hydraulic scaled model, a calculation according to the relevant similarity laws is of immense importance. For an application with free water surfaces, as it is the case in the suction chamber under consideration, modeling according to the Froude similarity, which shows a ratio of inertial force to gravitational forces, is suitable [31,32]:

$$Fr = \frac{v}{\sqrt{gD}} \tag{1}$$

In order to calculate the similarity, the Froude numbers of the original and the model must remain identical [31,32], where the characteristic diameter D describes the pipe diameter of the pump's suction line with $D = 0.082$ m for the model size:

$$\frac{Fr_M}{Fr_O} = 1 \tag{2}$$

When determining the scaling dimension, viscosity effects and surface tensions must be taken into account. By including the Reynolds number Re and Weber number We, scaling limits can be identified [6]. Inertial and viscous forces are considered using the Reynolds number Re:

$$Re = \frac{v \cdot D}{\nu} \tag{3}$$

The Weber number We is used to account for inertia and surface forces:

$$We = \frac{v^2 \cdot D \cdot \rho}{\sigma} \tag{4}$$

Recommendations for value limitations for the selection of these two key figures can be found in the relevant literature. According to [6,33], the Reynolds number should be in a range of $Re > 3{\cdot}10^4$, and the Weber number should be greater than $We > 120$. An additional safety factor of 2 is recommended for both values. The geometrical similarity must likewise be maintained. In this context, all dimensions of the systems under consideration must be in a fixed ratio to reach other [31]:

$$M = \frac{L_M}{L_O} = const. \tag{5}$$

Table 1 provides the conversion of various dimensioning parameters between the model and the original.

Table 1. Froude similarity scaling rules [32].

Parameter	Conversion	
Lengths	$L_O L_M^{-1}$	$= M$
Areas	$A_O A_M^{-1}$	$= M^2$
Velocities	$v_O v_M^{-1}$	$= \sqrt{M}$
Times	$T_O T_M^{-1}$	$= \sqrt{M}$
Flow rates	$Q_O Q_M^{-1}$	$= \sqrt{M^5}$
Forces	$F_O F_M^{-1}$	$= M^3$

2.2.2. Suction Chamber Test Rig Design

After applying the design parameters presented in advance, a scaling factor M of 3.66 was selected. In order to be able to observe comprehensive sedimentation investigations, the suction chamber was constructed out of transparent polyvinyl chloride (PVC) and

methyl methacrylate (PMMA). In addition, a water supply network with a water supply tank and speed-controlled pumps were implemented to enable different flow rates and water levels in the modeled suction chamber. A particle injection and filter were installed as well. All components assembled form the test rig are shown in Figure 2.

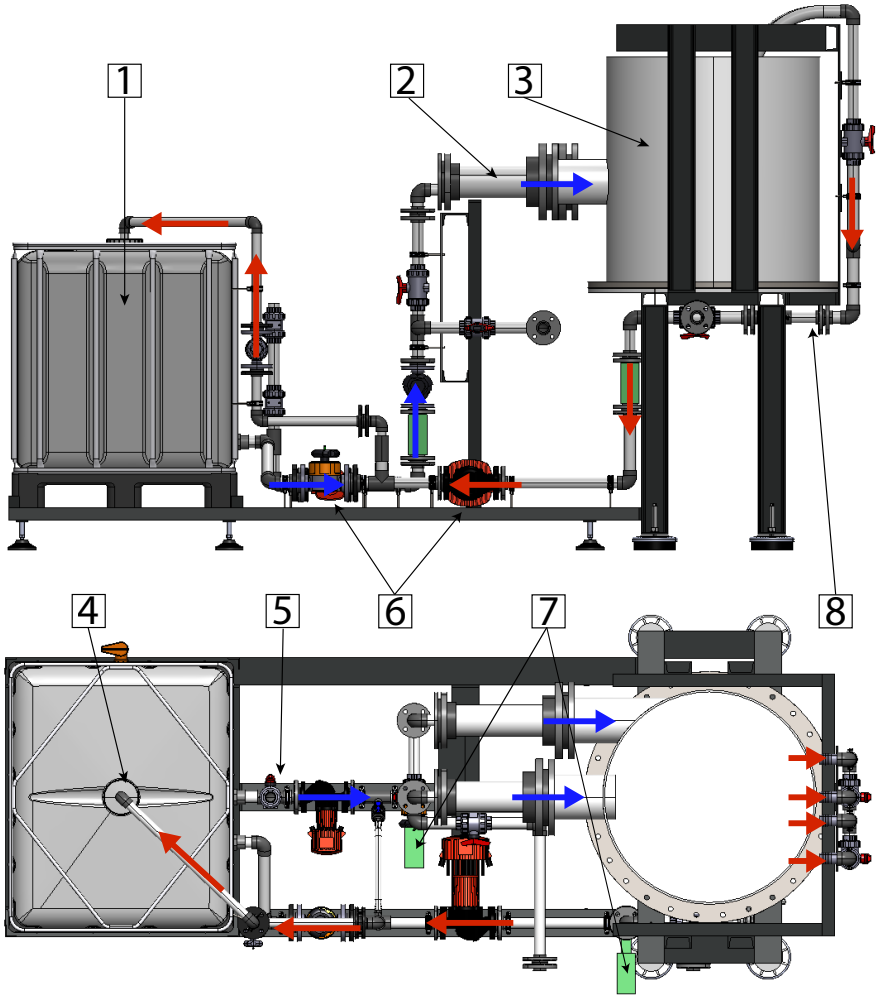


Figure 2. Suction chamber test rig.

The components shown in the graphic include (1) the water supply tank, (2) the inlet pipe into the model tank, (3) the model tank, (4) the particle filter, (5) the particle injection chamber, (6) the pumps, (7) the magnetic-inductive flow meter, and (8) the suction pipe exiting the model tank. With separately controlled inlet and outlet lines equipped with their own pumps, it is possible to set independent flow rates and operate at different water levels. Using the two tanks and the filter units, particles can be added for each experiment and removed from the test unit again. This allows for an assessment of the amount of sediment carried away by the flow. The inlet line is designed so that it can be connected to the test tank via a tangential or radial inlet. The inlet line is marked with blue arrows in the diagram. The outlet line can operate in single or parallel mode to draw fluid from the test tank at the designated positions and return it to the storage tank via the filter section. The outlet line is marked with red arrows in the diagram. The inlet and outlet pipes as well as the pumps are fitted with additional connecting pipes to ensure the dispensing of air of the individual lines. The selected scale of the model tank is shown in Table 2.

Table 2. Model suction chamber properties.

Parameter	Value
scaling factor M	3.66
diameter D	0.93 m
height h	1.46 m
volume V	0.99 m^3
amount of pumps	3

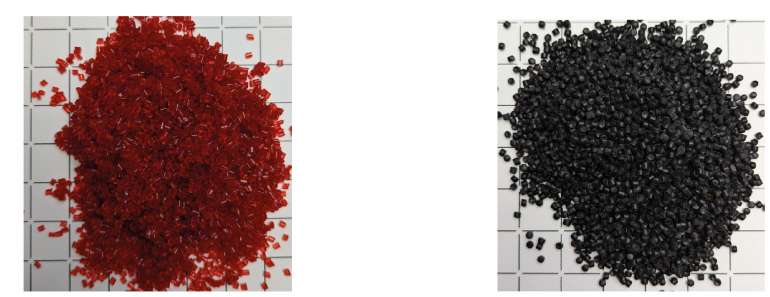
2.2.3. Replicating Sediments Contained in Wastewater

The composition of particles in wastewater systems has been subject of numerous studies. Crabtree [1] created a classification of different sediments, which was expanded by Kirchheim [2]. Further investigations regarding the wastewater medium were conducted by Mitchell [3]. Table 3 shows a selection of the particles found in sewer systems.

Table 3. Selection of wastewater particles.

Label	Density ρ [kgm^{-3}]	Particle Size p [mm]
gravel, sand, and sludge	1000–2150	0.4–15.0
fine sand	1230–2000	0.5–9.0

As the sources describe very high deviations in the weight and density of the respective particles, depending, for example, on the time of year and the catchment area, different colored plastic granules were selected to illustrate the different particle behavior. The red granulate shown in Figure 3a has a density of 1080 kgm^{-3} and replicates fine sand. The heavier black granulate is shown in Figure 3b and has a density of 1470 kgm^{-3}, thus representing heavy particles.



(**a**) light granulate (**b**) heavy granulate

Figure 3. Granulates used to replicate sediments in wastewater.

The purpose of the particles used is not to achieve an accurate representation of wastewater, due to its high deviation of particles, but to identify zones with average high sediment accumulations. By using two different types of particles, it is easier to visualize the deposition areas of lighter and heavier sediments. Optimization of these areas can be achieved in subsequent steps.

2.2.4. Test Procedure

The test sequences are based on a realistic pumping station operation. The inlet flow rates and pump flow rates are applied based on the average daily hydrograph. The average dry-weather discharge Q_A, the expected dry-weather peak Q_p and the maximum flow rate during a rain event with mixed water inflow Q_{max} provide the operating points under

consideration. The scaled values of the inflow, respective pump flow and the corresponding activation and deactivation levels of the two expansion stages can be found in Table 4.

Table 4. Flow rates and water levels.

Expansion Stage 1	Q_A	Q_p	Q_{max}
inflow [ls^{-1}]	0.71	1.24	2.49
outflow [ls^{-1}]	1.99	1.99	2.40
activation level [m]	0.22	0.22	0.30
deactivation level [m]	0.11	0.11	0.11
Expansion stage 2			
inflow [ls^{-1}]	1.24	3.11	4.56
outflow [ls^{-1}]	3.00	3.00	4.40
activation level [m]	0.27	0.36	0.42
deactivation level [m]	0.11	0.11	0.11

At the respective operating point, a constant inlet flow rate fills the model tank. When the defined activation level is reached, the respective pump is switched on and discharges water from the tank until the water level reaches the deactivation level. Filling and draining the tank between these two levels is referred to in the following as a pump iteration. When carrying out experiments, defined quantities of red and black particles are added to the inlet flow and are collected again with a filter unit at the end of the test rig. Amounts of 420 g red particles and 267 g of black particles, which correspond to poured volumes of 600 mL and 300 mL in the respective cases, are used. Particle injection takes place in the active inlet flow during the first pump iteration. After a thorough review phase, the maximum number of pump iterations was set to 10. In almost all cases, particle movement could hardly be observed after the intervals had elapsed. If all particles are removed from the model tank before the tenth pump cycle is reached, it is regarded as a stop criterion. At the end of the test, the black and red particles are removed from the filter, separated, dried and then weighed. In addition to the validation of the discharged particles, remaining sediments in the model tank are documented. To ensure a precise description of deposition formation, the base of the test setup was marked as illustrated in Figure 4. These investigations help to understand the basic behavior of the pump sump and to identify the isolated influence of flow rates and water levels on the particles.

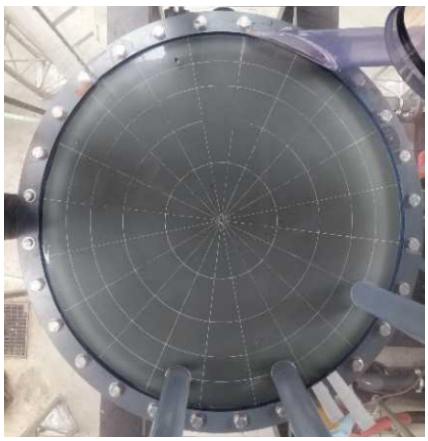


Figure 4. Marked model tank base.

2.3. Results

2.3.1. Modification A

As shown in Figure 5, modification A is the implementation of the concept of a suction chamber with a central cone presented in Figure 1. Figure 6 shows the sketched particle deposits after ten pump iterations during operation in expansion stage 1. As depicted in Figure 6a, both the lighter red particles and the heavier black particles sediment immediately after reaching the sump pump. The detachment of some particles and the movement along the clockwise direction, i.e., against the intended flow direction in the channel to the pumps, can be seen. During operation, the suction flow of the pump dominates and activates a part of the sedimented particles. In Figure 6b, when using a higher flow rate of Q_p, the activation of red particles towards the pumps can be seen. However, due to the channel flow that appears, sedimentation zones form again in the area of the cone, which cannot be broken down. Nevertheless, the flow conditions in the sump pump are not yet sufficient to activate the black particles. As expected, the best effect can be observed during a rain event with a flow rate of Q_{max} depicted in Figure 6c. Both types of particles were almost completely removed. Figure 7 shows the discharge particle quantities in percent of the respective investigations.

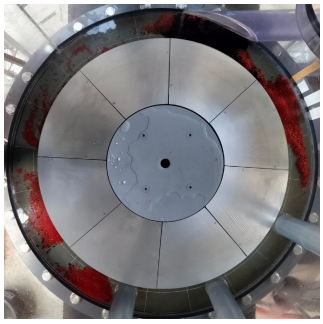
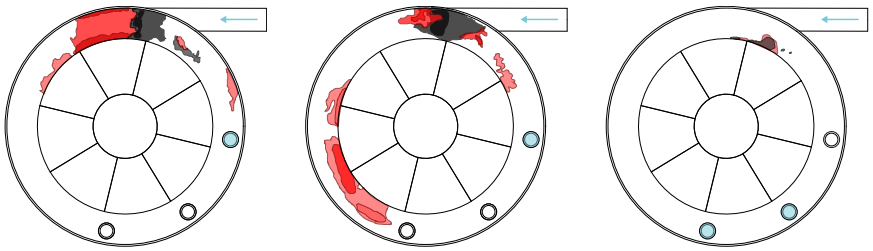


Figure 5. Round suction chamber with a central cone.



(a) Q_A **(b)** Q_p **(c)** Q_{max}

Figure 6. Particle depositions in expansion stage 1.

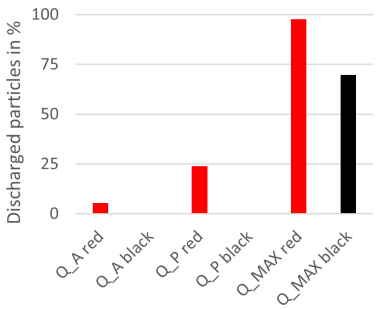
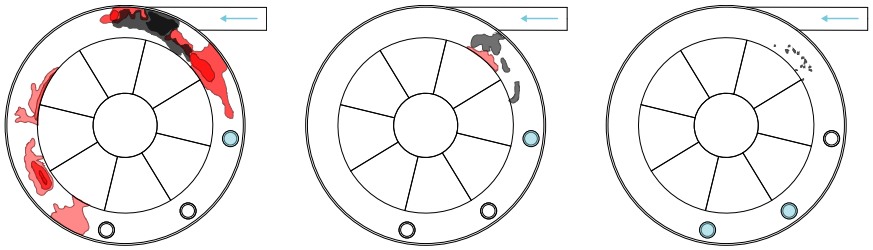


Figure 7. Percentage of discharged particles at expansion stage 1.

For the subsequent expansion stage 2 with a higher flow rate, a significantly better movement of the particles can be observed compared with expansion stage 1. During operation at Q_A in Figure 8a, activation of the light sediments can already be seen. However, the heavier black sediments still did not reactivate. Significantly higher discharge quantities of particles were achieved in operation at Q_p as shown in Figure 8b. As in the previous expansion stage 1, almost all particles could be discharged from the model at the high-flow rate Q_{max} during a rain event, as illustrated in Figure 8c. Significantly better removal of the particles in expansion stage 2 is also underlined by the increased discharge quantities shown in Figure 9.

In the course of further investigations, several additional concepts were developed and examined. These include, among other things, test series with different pump positions, eccentric cone placement and increased cone diameter. Even though some of the measures listed were able to remove higher quantities of particles, it was not possible to achieve a conversion with complete particle removal after ten pump iterations in any of the test series. For this reason, a fundamentally different modification was implemented.



(**a**) Q_A (**b**) Q_p (**c**) Q_{max}

Figure 8. Particle depositions in expansion stage 2.

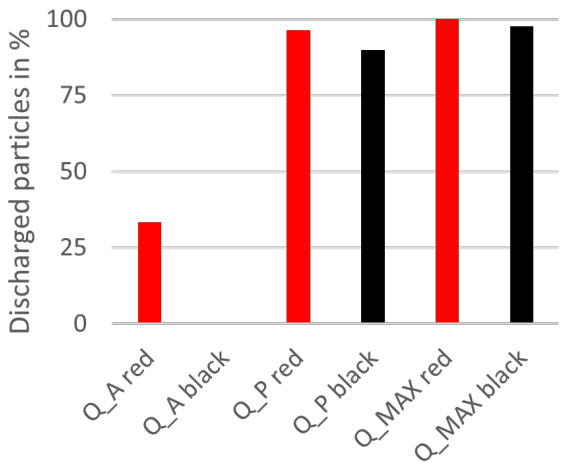
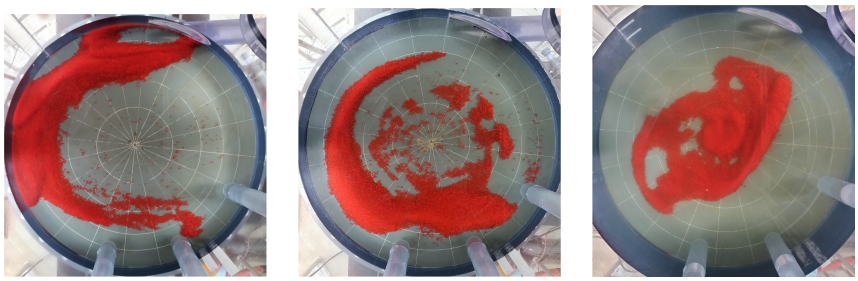


Figure 9. Percentage of discharged particles at expansion stage 2.

2.3.2. Modification B

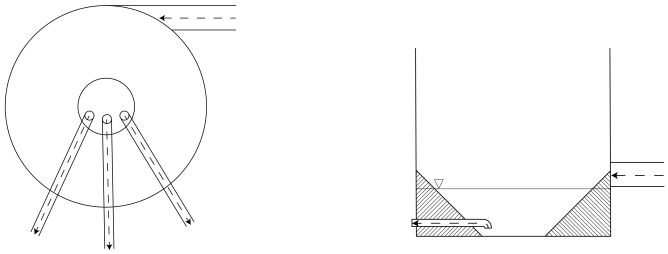
Modification B follows the approach of making maximum use of the vortex created by the tangential inflow and the particle transport it supports. Figure 10 shows the particle transport for Q_A in Figure 10a, Q_p in Figure 10b and Q_{max} in Figure 10c without built-in sloped walls. Even without installations, a clear movement of the particles towards the center of the model tank can be observed.



(**a**) Q_A (**b**) Q_p (**c**) Q_{max}

Figure 10. Particle transport with tangential inflow.

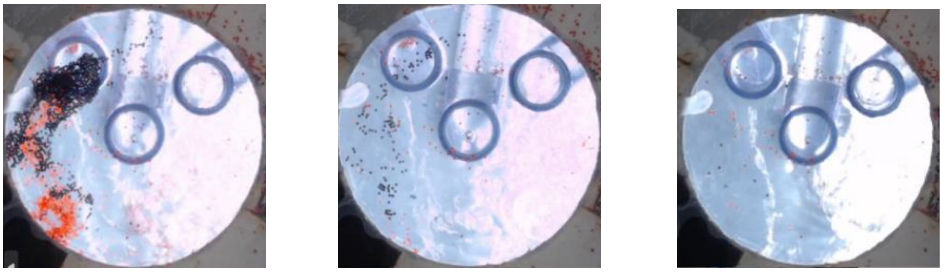
Based on this idea, a circular suction chamber with three dry-installed pumps was developed, in which the pump positions are shifted by 45°. Movable pipes make it possible to vary the positions of the individual suction intakes and to investigate different considerations, such as a central suction intake or three intakes at an identical distance from the center. The distance from the inlet bottom of the suction pipes to the bottom of the tank is D/2. Figure 11 shows the design layout with a top view in Figure 11a and a sectional view in Figure 11b.



(**a**) top view (**b**) sectional view

Figure 11. Design of Modification B.

The investigations with the new sump pump design started with the test series of expansion stage 1 with the lowest flow rate Q_A. All particles were discharged from the suction chamber after just the third pump iteration. Figure 12 provides a view from below the model tank after one, two and three pump iterations in Figure 12a–c, respectively. The high discharge performance was maintained across all test scenarios at the operating points Q_A, Q_p and Q_{max} for both expansion stages 1 and 2.



(**a**) after 1 pump iteration (**b**) after 2 pump iterations (**c**) after 3 pump iterations

Figure 12. View from below the model tank at flow rate Q_A.

2.4. Discussion

Modification A showed good results in terms of removing the particles at higher flow rates Q_{max} and partially good results at Q_A. However, with the exception of rain events, it was never possible to completely remove all particles within ten pump iterations. Even further optimizations of modification A could only show partial improvements. The use of

modification B resulted in a significant increase in particle removal. Even at expansion stage 1 at flow rate Q_A, it was possible to achieve early test termination due to complete particle discharge. In further investigations, an adjustment of the activation and deactivation levels as well as a flow simulation of the sump pump should be aimed for.

3. Influence of Cut-Back Leading Edges on Efficiency and Functionality

The previous section presents measures for the optimization of the suction chamber of a round wastewater pumping station. Specifically, the design is optimized to improve the transport of solids from the suction chamber, through the wastewater pump and to subsequent processing facilities. Therefore, in the case that the applied pumps are needed for the transport of contaminants, the pumps themselves, specifically the impeller and housing, need to be designed so as to exhibit low susceptibility to clogging. This goal is demonstrated here for a semi-open two-channel impeller by first designing an impeller optimized for efficiency and subsequently adapting the design for functionality, i.e., reducing the impeller's susceptibility to clogging.

3.1. Materials and Methods

3.1.1. Design of Optimized Impeller

The impeller for the investigation is designed as a semi-open two-channel impeller. For this purpose, a basic impeller is designed, which is then optimized by means of response surface optimization (RSO) to obtain a maximum clear-water efficiency. For this basic impeller design, the flow rate Q is selected as 400 m^3/h at a head H of 24 m for the design point. With a design speed n of 1487 min^{-1}, the specific speed n_q results in 45.7 min^{-1}.

In order to be able to estimate the attainable target for the efficiency-optimized impeller, the expected maximum efficiency is first considered. Based on [34], a single-stage, single-suction volute casing pump achieves a maximum clear-water efficiency η_{Pump} of approx. 89% at a flow rate Q of 360 m^3/h and a specific speed n_q of 45 min^{-1}. As this is a wastewater impeller with only two blades, the efficiency factor according to [9] for two-channel wastewater impellers is used. This factor varies between 0.8 and 0.98. Therefore, the clear-water efficiency η_{Pump} results in an expected efficiency range between 71 and 87%. However, it should be emphasized that this estimate covers both semi-open and closed two-channel impellers. Since semi-open impellers have lower efficiency than closed impellers due to the lack of a shroud and the resulting gap between the tips of the impeller blades and housing, efficiency values up to 80% are assumed on the test rig.

In addition, boundary conditions are defined for the design impeller that remain unchanged during the RSO. The outlet diameter and the outlet width of the impeller are defined and adapted to the existing volute. This volute is used because previous tests have already shown that its design is not susceptible to clogging. The volute casing has a suction side diameter of 200 mm with a discharge side size of 150 mm. In addition, the impeller is required to have three-dimensional blades that can be varied for both the inner and outer streamlines as part of the optimization process. As the bearing housing for the volute casing is already present, the dimensions of the impeller screw are also predetermined. The blade thickness is 10 mm and is also kept constant across all optimization variants. The blade leading edges for the optimization have an elliptical profile at each sample point.

Impeller Optimization. For the setup of the RSO, the basic impeller is selected. The volute casing used for the simulation is redesigned based on the existing volute casing and contains the same cross-sectional profile.

The simulations of the basic design and the RSO are carried out as stationary simulations using RANS-equations in a coupled solver with CFX software. The high resolution scheme is used for numerical discretization and turbulence numerics, using second order

central differencing. The SST model is used for turbulence modeling in order to achieve good resolution and convergence both in near-wall areas and free streams [35]. The impeller and the volute casing are meshed with unstructured meshes and given prism layers on the corresponding walls as well as blades. A dimensionsless wall distance between 30 and 50 is used for the impeller and volute casing, whereby logarithmic wall laws are used. The impeller is calculated as a closed impeller, which means that the gap between the tips of the blades and the frontliner used later in the experiment is not calculated. Furthermore, the impeller back shroud cavity is also not considered in the simulation. In addition, the domain is given an inlet pipe in front of the suction side of the impeller and an extension on the volute casing. Both pipes are treated as frictionless and are also unstructured meshes. Stationary coupling models between the rotating impeller and the inlet pipe as well as the volute are used in which the flow variables are transferred axially averaged between the domains. For the convergence criterion, the residuals are set to 10^{-5} by using root mean square (RMS).

For the simulation with the basic impeller and the geometrically similar volute casing, a mesh independence analysis is first carried out, which contains a coarse, a medium and a fine mesh for the impeller. The results of efficiency are shown in Figure 13.

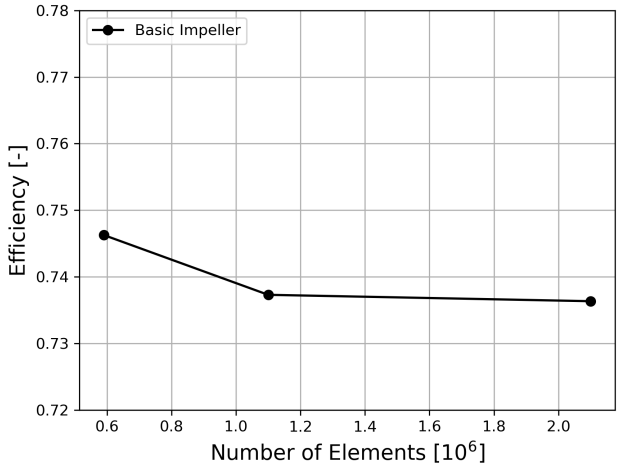


Figure 13. Mesh independence analysis.

As can be seen in Figure 13, the deviation in efficiency between the medium and fine meshes is 0.13%, which is why the medium mesh is used for RSO. The sample method for RSO is Latin hypercube sampling (LHS). This is due to the fact that LHS ensures that each parameter is represented in a full manner [36]. For the LHS method, 200 samples are used for the design of experiment (DOE).

A total of ten parameters of the impeller are changed as part of the optimization. Five parameters are selected equally for both the outer (shroud) and inner (hub) streamline. These include the blade angle of the leading edge β_1; the blade angle of the trailing edge β_2; the relative starting position of the leading edge u, which influences the diameter of the leading edge accordingly; and starting from a common baseline, the wrap angle of the leading edge ϕ_1 and the wrap angle of the trailing edge ϕ_2. The parameters vary from the basic design in the direction of both higher and lower values. Figure 14 shows the varied parameters, illustrated using the example of the designed basic impeller the RSO.

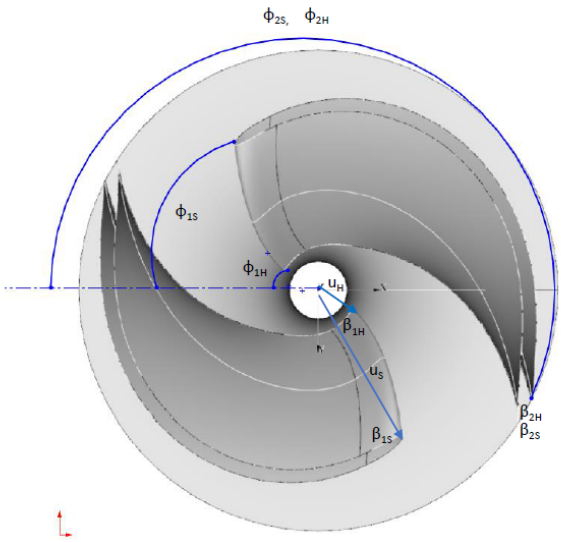


Figure 14. Parameters for DOE.

The head H and the efficiency η_{Pump} of the simulated impeller are used as output parameters. The focus here is on maximizing efficiency, while the head plays a subordinate role.

Figure 15 shows the results of the DOE. The sensitivity of the individual varied parameters in relation to the basic impeller with regard to the influence on the efficiency is shown.

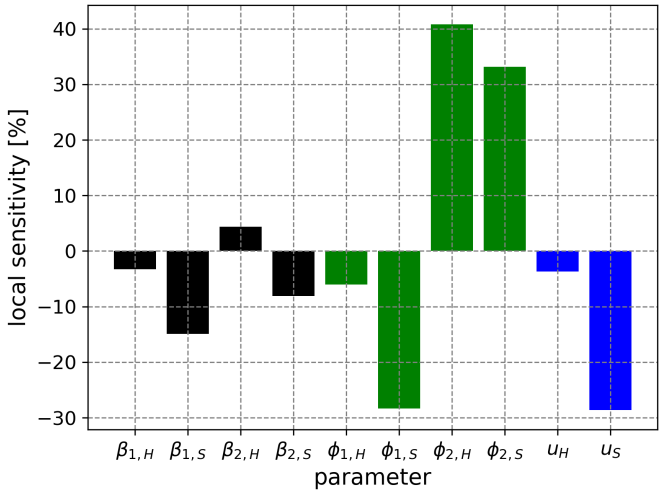


Figure 15. Local sensitivity analysis for η_{Pump}.

Figure 15 shows in particular that increased wrap angles at the outlet ϕ_{2H} and ϕ_{2S} have a significant positive influence on the efficiency of the impeller. In contrast, increased wrap angles at the inlet ϕ_1, especially on the outer streamline ϕ_{1S}, have a negative effect on the efficiency of the basic impeller. The blade angles at the inlet $\beta_{1,H}, \beta_{1,S}$ and outlet $\beta_{2,H}, \beta_{2,S}$ have a subordinate influence. In addition, the position of the leading edge on the outer streamline u_S is decisive for the efficiency of the impeller, while the position of the leading edge on the inner streamline u_H has a minor effect on efficiency. Especially for the outer streamline, increased starting positions, which correspond to increased diameters, lead to a significant reduction in efficiency. This also indicates that longer blades that start directly at the suction side of the impeller increase efficiency for this application.

Based on the individual sample points, it can be seen that particularly high wrap angles lead to high efficiency. As different blade geometries are to be examined in the

further course of the investigations, a target value for a wrap angle at the trailing edge is specified for optimization in addition to a target value for maximum efficiency. This wrap angle target value is also selected to be the same for both the inner and outer streamlines of the blades, as a two-dimensional trailing edge is desired. The latter is because the use of different blade inlet geometries would otherwise result in unwanted narrow passages between one leading edge and the other blade. The requirements for optimization are therefore maximizing efficiency as well as achieving a wrap angle at the trailing edge ϕ_2 of 210° for both streamlines.

For optimization, non-dominant sorting genetic algorithm II (NSGA-II) is used as an optimization algorithm. The selected candidate for optimization meets the boundary conditions of an almost-two-dimensional trailing edge with a maximum wrap angle for the end of the blade of approx. 210°. Overall, the impeller has a wrap angle of 189° per blade. In addition, there is a maximum efficiency of 84.2% for NSGA-II, which results in a simulated efficiency of 83.6% in the geometrically similar volute for optimization. Due to the range for the estimated efficiency for the semi-open two-channel impeller, the candidate for the prototype is chosen as the basic modification (MOD 0) for the prototype.

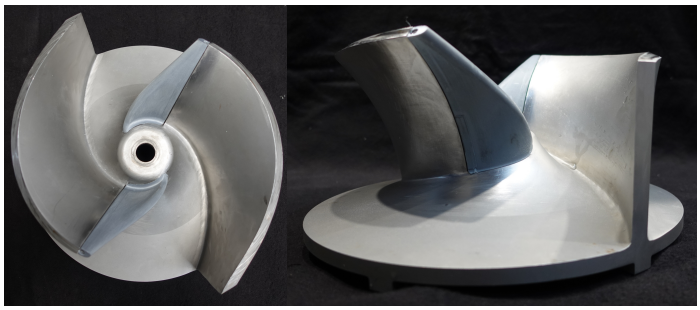
Prototype Manufacturing. In order to test both the optimized blade geometry and cut-back variants of this blade, a stainless steel prototype is manufactured. This is designed according to the optimized blade contour given by the RSO. In order to be able to test different leading edges in one prototype, the leading edge of the optimized contour for the stainless steel impeller is cut off by 40% of the outlet diameter and provided with holes on the hub and shroud to which the different leading edges can be screwed as modifications, which are manufactured via 3D printing. The materials used for the leading edges are polycarbonate (PC) for the optimized blade leading edges (MOD 0) and polylactide (PLA) for the other modifications (MODs 1–2). PC offers increased strength, which is necessary due to the long contour of the optimized blade leading edges, especially regarding the outer streamline. PLA allows for fast and cost-efficient printing.

To ensure that the impeller has the same gap width of 0.3 mm between the blades and frontliner despite different modifications, an adapter plate is also used, which is screwed onto the back of the stainless steel impeller. This adapter plate holds the shaft–hub connection and represents the same installation situation on the shaft. The frontliner has one groove in all tests, which is used to convey the dusters.

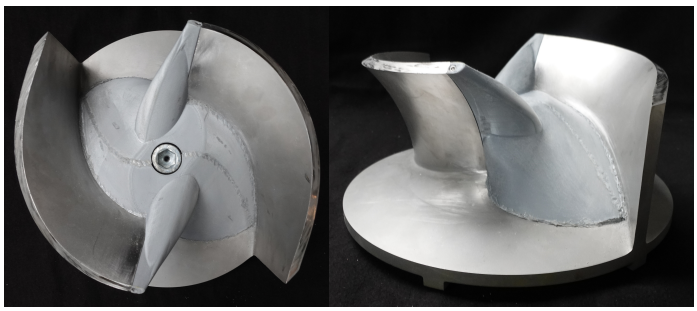
Impeller Variation. A total of three modifications are used for the impeller in this publication. On the one hand, the blade leading edges resulting from the RSO are used as modification 0 (MOD 0), which forms the baseline for the efficiency and functionality measurements. On the other hand, cut-back blade leading edges are implemented, which have the aim of increasing the functionality by slipping off the dusters on the leading edge, while the efficiency is to be maintained. In the first step, the outer streamline of the leading edge is cut back to 40% in length in relation to the outlet diameter of the impeller, while the inner streamline is unchanged to achieve a resulting curvature between both streamlines. The blade thickness and the elliptical profile remain unchanged. This first modification is continuously described as MOD 1. In addition, starting from MOD 1, the blade leading edges are thickened to 40 mm on the inner streamline in the direction of the impeller screw, which should enable improved slippage. This thickening tapers towards the outer streamline to the thickness of the original blade. In addition, the hub area is reworked to create a plateau between the blades. This plateau is created because previous tests have not only shown severe clogging at the leading edges but also clogging at the screw and hub geometry. This second modification is continuously referred to as MOD 2. Figure 16 shows the individual modifications installed in the stainless steel prototype.



(**a**) MOD 0: optimized contour



(**b**) MOD 1: 40% cut-back leading edge



(**c**) MOD 2: thickened inner streamline

Figure 16. Tested impeller modifications.

3.1.2. Test Rig Setup

The chair of Fluid System Dynamics at Technische Universität Berlin operates a designated test rig for the standardized testing of wastewater pumps.

Test Rig and Procedure. Figure 17 shows the test rig used to carry out the standardized wastewater tests. The test rig is composed of two 4 m^3 tanks that are connected through looped pipes, integrating the pump under test. The various valves enable the configuration of different circuits to move the water. For the standardized testing, water is pumped in a circle from and to the wastewater tank. The test medium is artificial wastewater consisting of clear water mixed with dusters. These dusters have a size of 22 $\times$ 33 cm with a fabric weight of 60 g/m^2. They have been found to most closely reproduce the clogging phenomena observed in wastewater pumps in the field induced by nonwoven wipes [11,37]. The standardized test is called the long-time functional performance test, where the artificial wastewater is pumped in a loop for the duration of an hour. The operation of the motor, and thus the pump, is facilitated with variable-frequency drive (VFD). The VFD is set to maintain constant speed of rotation.

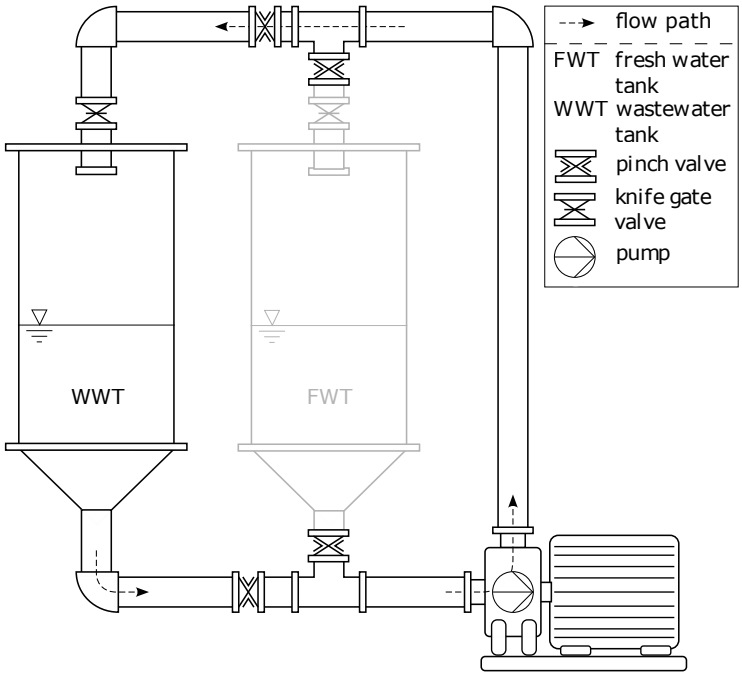


Figure 17. Schematic of the test rig and the flow paths [38].

After a test, the pump is opened to retrieve the dusters clogged in the impeller of the pump. With this, the weight ratio of all dusters introduced in the test and the ones remaining clogged in the pump at the end of the test is determined. This weight ratio assumes a value of 1 when all introduced dusters are clogged inside the pump at the end of the test. Oppositely, a weight ratio of 0 implies that all dusters have been continuously pumped without being accumulated in the pump at the end of the test. This test can be repeated for three different so-called contamination classes. These modify the number of dusters introduced in the test in steps of 25, 50, or 100 dusters per cubic meter of water.

For each long-time functional performance test of a pump, the so-called degree of long-time functional performance (D_{LTF}) is calculated according to the following equation [28]:

$$D_{LTF} = \frac{1}{2} \cdot \frac{\overline{\eta}}{\eta_{CW}} + \frac{1}{2} \cdot \frac{m_{w,total} - m_{w,pump}}{m_{w,total}}, \tag{6}$$

where $\overline{\eta}$ is the average efficiency of the test, η_{CW} is the efficiency of the pump in clear-water operation and $m_{w,\_}$ are the weights of the total dusters introduced in the test and of dusters remaining in the pump at the end of the test.

In addition to the long-time functional performance tests, a clear-water reference measurement of 30 s is recorded for each operating point of the pump under test. The obtained clear-water values serve as a reference for the changes in the hydraulic, mechanical, and electric characteristics which are induced in the long-time functional performance tests due to wastewater operating conditions and potential clogging.

Sensor Setup. In order to analyze the operation of the pump under wastewater conditions, several measurements are carried out to determine important performance metrics. The differential pressure is measured between the inlet and outlet of the pump, according to DIN EN ISO 9906 [39]. The flow is determined with an inductive flow meter. These measurements enable the calculation of the pump head. The test rig is additionally equipped with a torque transducer to measure the torque and rotational speed of the pump. The torque transducer has high accuracy with a maximal measurement error of 0.03%. This enables the precise determination of the mechanical power supplied to the pump and

therewith the calculation of pump efficiency. All measurements are recorded at a sampling frequency of 1 Hz.

3.2. Results

3.2.1. Analysis of Efficiency

Figure 18 shows the results of both the simulated point of the selected optimization candidate with geometrically similar volute and the clear-water measurements of MOD 0–MOD 2 on the test rig.

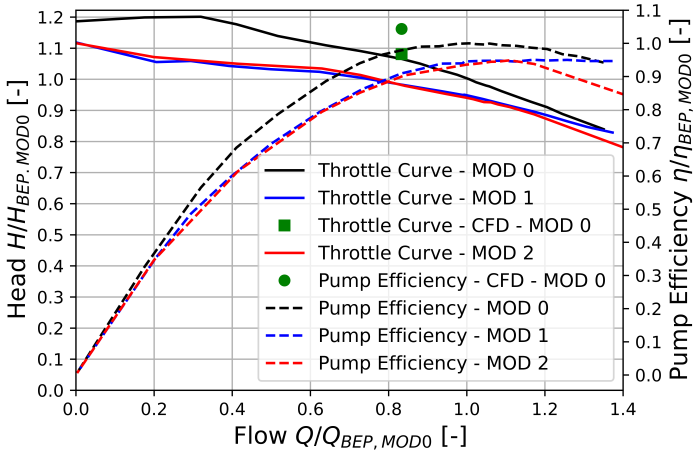


Figure 18. Clear water results for MODs 0–2.

When comparing the CFD results for the optimized geometry with a geometrically similar volute to the clear-water measurement with the given volute, it is striking that the simulated head of 27.8 m is almost achieved by the clear-water measurement for MOD 0. Nevertheless, it can be seen that the simulated efficiency of 83.6% is not achieved. For the clear-water measurement of MOD 0, the BEP has increased in the direction of higher flow rates compared with the design flow rate at a flow rate Q of 480 m^3/h, a head H of 25.7 m and a clear-water efficiency of η_{Pump} 80.1%. Accordingly, the simulated maximum efficiency is relatively above the measured result, by 4.4%. This can be related to the assumptions made for the simulation, meaning the use of a stationary simulation without a gap between frontliner and blade tips as well as the lack of the back shroud cavity. In relation to the expected range for maximum efficiency presented in Section 3.1.1, the results of MOD 0 are within the expected scope.

The clear-water results for MOD 1 and MOD 2 each show a reduction in the head H above the flow rate Q due to the shortened blades. In addition, it can be seen that the throttling curves of MOD 1 and MOD 2 are nearly similar, meaning that the thickening of the inner streamline of the blades and the covering of the impeller screw have a subordinate influence on the hydraulic performance of the impeller in contrast to the blade length. It is also noticeable that cutting back the blade leading edge shifts the BEP of the individual modifications in the direction of higher flow rates. The maximum efficiency of MOD 1 and MOD 2 is always below the efficiency of MOD 0 due to the modifications of the blade and result in 94.8% for MOD 1 and 94.9% for MOD 2 compared with MOD 0. Due to the shift towards higher flow rates, the heads of the two modifications with a shorter blade leading edge are correspondingly lower in the BEP compared with MOD 0, while the mechanical power is higher. Table 5 shows the values of the BEP in relation to MOD 0.

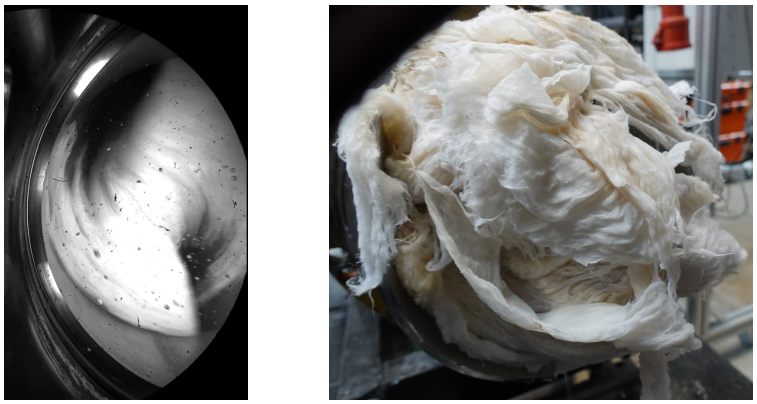
Table 5. BEP results for MODs 0–2.

MOD	0	1	2
$\eta/\eta_{MOD\,0}$	1.000	0.948	0.949
$Q/Q_{MOD\,0}$	1.000	1.083	1.104
$H/H_{MOD\,0}$	1.000	0.922	0.911
$P/P_{MOD\,0}$	1.000	1.050	1.059

3.2.2. Analysis of Functionality

For all modifications, long-time functional performance tests with low contamination L25 at the BEP and optical examinations at the BEP were carried out and compared.

MOD 0: The long-time functional performance test with low contamination for MOD 0 was aborted after approx. 280 s of measurement due to blade breakage of one of the two PC blades. Despite the very short measuring time, a total of 283 g of 283 g of dusters were collected inside the impeller. This resulted in a $D_{LTF,L25,MOD\,0}$ of 0.24 with an average normalized pump efficiency during the test of 47.3%. Even after the short measurement period, this reduced efficiency resulted from an increase in mechanical power to 111.8% compared with their clear-water value, while the flow rate dropped to 78.9% and the head to 66.1% compared with the clear-water values. The clogging pattern within the impeller after the test and the findings of the optical tests in particular explain why the hydraulically optimized contour is not suitable for media containing fibers. The individual dusters are layered over the leading edges so that subsequent dusters accumulate on them. The blade leading edge, which does not have a sloping edge between the inner and outer streamlines, prevents the dusters from slipping off. Figure 19a shows an image from the optical test. It can be seen that both blades are covered by dusters. This blockage grows together over the hub area and covers the impeller screw. Figure 19b shows the clogging pattern after the long-time functional performance test has been stopped.



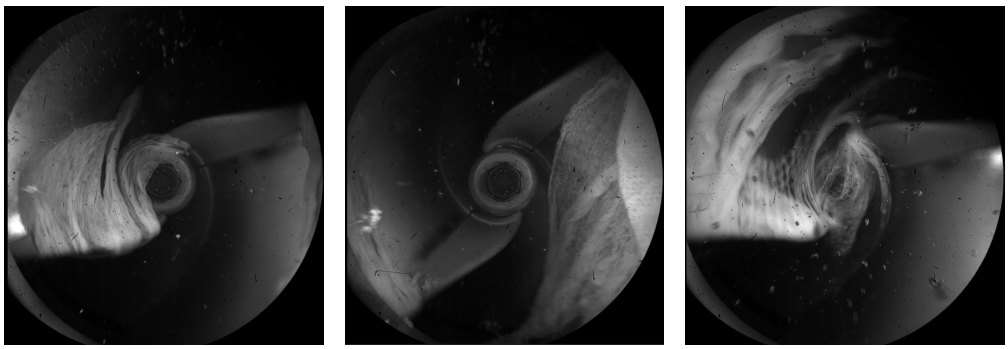
(**a**) (**b**)

Figure 19. Results for MOD 0 from optical investigation and after-test inspection. (**a**) accumulation on hub and leading edge; (**b**) blockage inside impeller for L25.

MOD 1: The optical tests with 10 dusters per cubic meter showed improved slipping behavior of the dusters at the leading edges of the blades, as shown in Figure 20.

Figure 20a shows a duster that lies on one of the two leading edges. Due to the cut-back of the outer streamline of the blade and the resulting curvature between the outer and inner streamlines, the duster slid along the blade in the direction of the frontliner. Figure 20b shows the same experiment after approx. half a revolution. The applied duster moved in the direction of the outer streamline and ultimately slipped towards the suction side of the blade, which shows an improvement compared with MOD 0.

However, the optical examinations also show a clogging-prone scenario of MOD 1. Dusters that hit the center of the impeller and thus directly on the hub and on the inner streamline of the blade were not removed and formed the beginning of an accumulation. Further arriving dusters were deposited on this initial blockage and grew together over the blades. This initial blockage is shown in Figure 20c, in which dusters are attached over the impeller screw and the inner streamline of the blade leading edge and are not discharged until the end of the optical measurement. The low blade thickness on the inner streamline in particular means that there is no slipping behavior in the optical tests, if the dusters already cover the screw.



(**a**) (**b**) (**c**)

Figure 20. Results for MOD 1 from optical investigation. (**a**) duster attached on leading edge; (**b**) duster slipping off into channel after half a revolution; (**c**) clogging on hub, leading edge and impeller screw.

This behavior is also reflected in the long-time functional performance test with low contamination class at the BEP. In this test, a total of 221 g of 284 g of dusters was absorbed by the impeller, which corresponds to an improvement compared with the clogging behavior of MOD 0. Over 60 min of measurement, MOD 1 achieved a relative average pump efficiency of 78.9% compared with clear-water operation, which is mainly due to increased mechanical power. This amounts to 115.0% compared with the clear-water value, while the flow rate of 97.0% and the head of 93.5% are close to clear-water operation. Overall, $D_{LTF,L25,MOD\,1}$ is 0.50, which is due to the improved hydraulic performance and the lower absorbed weight during the test. Figure 21 shows the clogged impeller after the end of the long-time functional performance test.

In Figure 21a the blockage of 221 g can be seen. Figure 21b shows that after lifting the accumulation of dusters, the blockage has grown together over the impeller screw, as could already be observed in the optical examination.

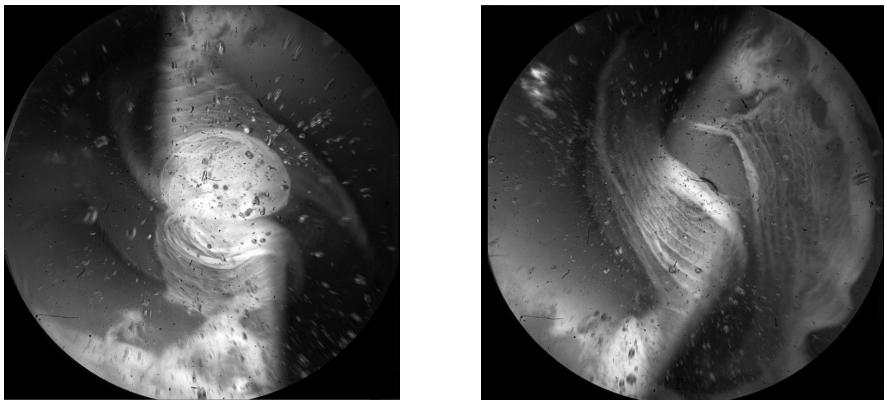
Overall, this results in a gain in functionality of 0.26 for MOD 1, even if this is accompanied by a relative drop in clear-water efficiency of 5.2% compared with MOD 0.

MOD 2: The optical investigations for MOD 2 show improved slipping behavior compared with the previous modifications. Figure 22a shows two dusters hitting the hub directly. As shown in Figure 22b, each of these dusters slipped into a blade channel after one revolution. The thickened inner streamline of the leading edge helped the dusters to slide either into the blade channel or in the direction of the outer streamline of the leading edge. The plateau which covers the impeller screw prevented the dusters from sticking on the hub, even though a relatively long dwell time of the dusters was recorded during the optical examinations. Due to the flat contour of the plateau, some dusters needed several revolutions to be conveyed from the hub towards the channel.



(**a**) accumulation of dusters (**b**) accumulation attached to impeller screw

Figure 21. Results for MOD 1 from after-test inspection for L25.



(**a**) (**b**)

Figure 22. Results for MOD 2 from optical investigation. (**a**) two incoming dusters on the plateau; (**b**) dusters slipping off into blade channels after one revolution.

The long-time functional performance test with low contamination L25 at the BEP shows a significantly better result compared with the previous modifications. After 60 min of measurement, no dusters had accumulated inside the pump. With an average relative efficiency of 95.5%, this resulted in a $D_{LTF,L25,MOD\,2}$ of 0.98, therefore above the required 0.7. The mechanical power was unchanged during the test compared to the clear-water value, and the hydraulic data show a minimal decrease due to the pumping of the textiles. This results in an average flow rate of 98.6% and a head of 96.8% compared with the clear-water values.

In addition, due to a result for $D_{LTF,L25,MOD\,2}$ greater than 0.7, the long-time functional performance test for MOD 2 was also carried out with medium contamination. In this case, a blockage of 395 g of a total of 572 g of added mass built up. With an average efficiency over the test duration of 60.7%, this resulted in a $D_{LTF,L50,MOD\,2}$ of 0.46. The flow rate dropped to 85.5% and the head to 75.9% of the clear-water values, while the mechanical performance increased to 107.0%. Images of the blockages after the end of the test with medium contamination can be seen in Figure 23.

This behavior can also be found in the optical tests. Individually arriving dusters slid to the outer streamline, where they were removed by the groove in the frontliner. Due to the fact that only one groove was used, the dwell time of the dusters on the blades was also too long here. If many dusters hit a blade, an accumulation built up on the entire leading edge, as can be seen on one blade on the left side of Figure 24. Sliding was no

longer possible with this accumulation, so the blockage grew together in the direction of the hub.

Overall, MOD 2 shows greatly improved clogging behavior compared with the previous modifications, with a result above the required 0.7 for low contamination while achieving similar clear-water efficiency to MOD 1. In order to further improve the clogging behavior especially for higher contamination classes, the hub geometry should be further revised to minimize the dwell time of the dusters. In addition, a frontliner with a higher number of grooves should be tested.



(**a**) clogging inside impeller (**b**) removed blockage

Figure 23. Results for MOD 2 from after-test inspection for L50.

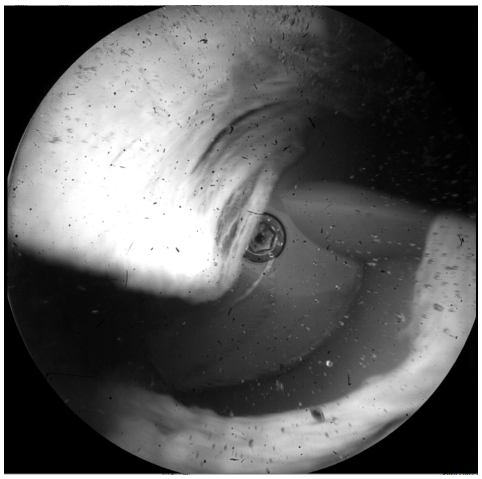


Figure 24. Results for MOD 2 from optical investigation: clogging scenario on one leading edge.

4. Influence of Back Shroud Cavity Housing Recess Geometry on Functionality

To ensure a reliable and environmentally safe transport of wastewater, it is insufficient to design a wastewater pump solely with the objective of achieving a high degree of long-time functionality according to Equation (6). This is due to the fact that even comparatively small amounts of fibers accumulated in the back shroud cavity can pose a risk to the operational safety of the mechanical seal.

4.1. Background

Hardly anything in a centrifugal pump has as powerful an influence on other essential components and operating behavior due to its design characteristics as the cavities

between impeller and housing. The flow prevailing there not only largely defines axial thrust [9,12]. It is furthermore well known that the shroud cavity design may also significantly affect radial thrust [9]. Besides axial thrust, the pressure within the back shroud cavity is also to be considered when choosing the shaft seal. With regard to pump efficiency, shroud cavity design impacts leakage losses and, in particular, disk friction losses [12,40]. The latter is nothing less than the fundamental motivation for the experiments on disks rotating in cylindrical housings, as conducted by Schultz-Grunow [41], Ippen [42] and Daily and Nece [43,44], from which the basic understanding of back shroud cavity flow is derived [9,12].

4.1.1. Enclosed Rotating Disk Flow

Based on analytical and experimental investigations on *enclosed rotating disk flow* conducted by Daily and Nece [43,44], it has become common practice to distinguish between the following four flow regimes, depending on the properties of disk and rear housing wall boundary layers:

I. Merged, laminar;
II. Separated, laminar;
III. Merged, turbulent;
IV. Separated, turbulent.

Reynolds number Re and axial gap width s_{ax} define the corresponding flow regime prevailing. However, surface roughness can increase boundary layer thickness and decrease the critical Reynolds number Re_c [43,44].

Within the disk boundary layer, the circumferential velocity is increased compared with the rest of the fluid. Directly on the rotating disk surface, the fluid moves with the local circumferential velocity of the disk itself, due to the no slip boundary condition. Accordingly, the no slip boundary condition causes the circumferential speed to be zero directly on the stationary rear housing surface. Compared with the rest of the fluid, the circumferential velocity is decreased within the rear housing boundary layer. Due to the increased circumferential speed within the rotating disk boundary layer, the fluid is therein centrifuged outward. Continuity enforces a radially inward-directed flow within the housing wall boundary layer, which leads to the characteristic radial–axial circulation between disk and rear housing wall. Together with the explained circumferential velocity distribution, this yields the three-dimensional flow around enclosed rotating disks. For sufficiently large axial gap widths s_{ax}, the boundary layers are separated from each other and a co-rotating rigid-body vortex develops between them [9,12,41,43].

Normally, flow regime IV is present in water pumps [9,12]. For the constellation of separated turbulent boundary layers, the radial velocities are always low compared with the circumferential velocities [9]. With regard to avoiding fiber entry into the back shroud cavity of a pump, this, together with the above-mentioned flow pattern, appears very convenient. It is tempting to assume that due to the continuous and isolated radial–axial circulation, fibers contained in the main flow could not enter the back shroud cavity. And even if fibers were to be near parts within the back shroud cavity that are to be kept free of them, it could be expected that they are once more circulated away. However, in reality, wastewater pumps have to be taken out of operation due to clogged back shroud cavities or destroyed mechanical seals.

4.1.2. Back Shroud Cavity Flow

In practice, the flow in the back shroud cavity differs considerably from the flow described for enclosed rotating disks. In both annular and volute housings, the velocity and pressure distribution is rotationally asymmetrical at all operating points, causing the

flow inside the back shroud cavity to be asymmetrical as well. Secondary flows through the back shroud cavity then occur as a result [7,9,45,46].

Furthermore, experiments and numerical simulations have shown that by actively dominating the flow through a suitable shroud geometry [45,46] or by passively protecting the respective shroud cavity [47], asymmetric flow within front or back shroud cavity can, to a certain degree, be homogenized.

For instance, Bubelach [46] applied front vanes to the front shroud of a wastewater pump with a closed one-channel impeller. Compared with the flat-disk-shaped front shroud configuration, the flow inside the front shroud cavity was less dependent on the circumferential pressure distribution in the annular housing.

Will et al. [45] numerically and experimentally investigated the flow inside the front as well as the back shroud cavity of a commercial standard pump with a single volute and a closed seven-channel impeller. Flow regime III was observed to prevail in the back shroud cavity due to low axial gap width s_{ax}. Viscous effects therefore had, to a certain degree, a homogenizing influence on the back shroud cavity flow.

Numerical and experimental investigations carried out by Knop et al. [47] showed that in addition to the pressure distribution in the housing, the pressure distribution in the impeller eye can also affect the flow in the front shroud cavity. The pressure field in the impeller eye was homogenized by adapting the impeller geometry, which prevented any further clogging of the one-channel wastewater impeller.

4.1.3. Housing Recesses

The extent to which the back shroud cavity is influenced by outer boundary conditions can be controlled by the design of the back shroud cavity, i.e., the design of the housing and the back shroud [9]. When the back shroud cavity is relatively open at the outer impeller diameter, the back shroud cavity flow is strongly coupled to the flow in the housing and the main flow behind the impeller outlet [9,45]. In contrast, when recessing the rear housing wall in a way that the radial gap width s_r is small, whereas the degree of back shroud coverage c_{BS} is high, the back shroud cavity flow can be decoupled from outer boundary conditions to a large extent [9]. The degree of back shroud coverage c_{BS} is determined as follows, using the parameters shown in Figure 25:

$$c_{BS} = \frac{d_{HR} - s_{ax}}{t_{BS}} \tag{7}$$

With regard to fiber entry, it is therefore expected that the discussed local, centripetally directed secondary flows in particular lead to an increase in fiber entry and thus to a decrease in functionality in open and accordingly strongly coupled back shroud cavities. It is vice versa assumed that with an increase in the degree of back shroud coverage c_{BS} and decreasing radial gap width s_r, the back shroud cavity flow is increasingly decoupled from the external boundary conditions stated above, thus decreasing fiber entry. It is of special interest for the investigation presented to obtain information on both the effectiveness and the corresponding magnitude of the parameters back shroud coverage c_{BS} and radial gap width s_r. Increased radial thrust is to be expected for increasingly decoupled back shroud cavity designs, as pressure-balancing secondary flows through the back shroud cavity are weakened [9].

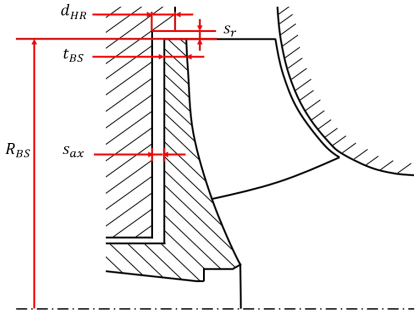


Figure 25. Back shroud cavity parameters.

4.2. Materials and Methods

4.2.1. Investigated Pump

The dry-installed wastewater pump investigated has a semi-open two-channel impeller with specific speed n_q and N_s at the best efficiency point (Q100) of 58.2 min^{-1} and 3005.2 min^{-1}, respectively. Its outer diameter is 277 mm. The impeller is modified in a way that different back shroud geometries can be mounted. Therefore, the original back shroud geometry was turned off and subsequently featured threaded holes. The investigated pump has a volute housing and is driven by a four-pole asynchronous motor at a constant rotational speed of 1490 min^{-1}. The rear housing wall is made of acrylic glass and hence fully transparent. It is furthermore equipped with threaded holes on different radii, so that the flat-disk-shaped rear housing wall can be modified.

4.2.2. Test Rig

Figure 26 shows the open-loop test rig operated for the experiments conducted. The water tank (WT) replicates a wastewater pumping station suction chamber. It has a capacity of 6 m^3 as well as fully transparent acrylic glass walls. During each test, artificial wastewater moves from the water tank through a DN250 elbow pipe into the DN150 suction line, where the static pressure upstream of the pump is obtained (PS). From there, the artificial wastewater is transported through the test pump (P) and the DN150 discharge line, where the static pressure downstream of the pump is measured (PP). From there, the artificial wastewater passes a shock diffuser and continues flowing through a magneto-inductive flowmeter (F). It subsequently passes a valve (V) installed for aeration as well as deaeration before passing the regulation valve (RV). Downstream, the artificial wastewater flows back into the water tank (WT).

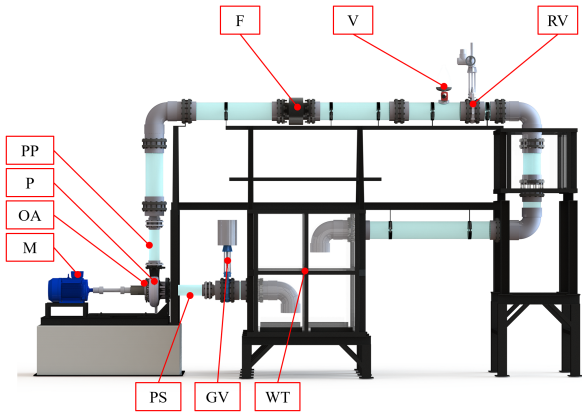


Figure 26. Test rig [21].

4.2.3. Replicating Fibers Contained in Wastewater

To replicate fiber content in wastewater, a defined quantity of microfiber rags is mixed with clear water in accordance with standard DWA-A 120-2 [5] and other works investigating the functionality of wastewater pumps, such as [14,26]. The *contamination class* chosen corresponds to 25 rags per 1 m^3 of clear water, which complies with the lowest loading class defined in [5]. The total amount of microfiber rags thus corresponds to 150 for each of the tests conducted.

4.3. Housing Recess Configurations

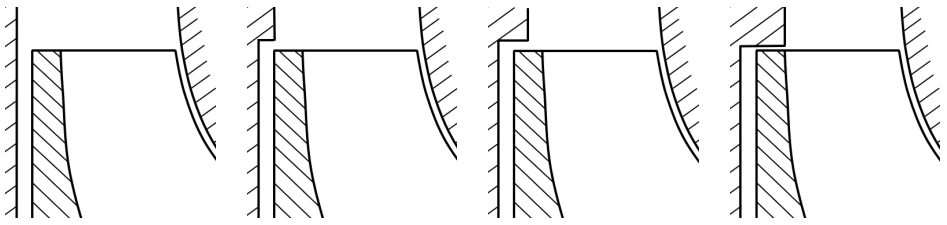
Figure 25 shows the main parameters relevant for the housing recess configurations. The axial gap with s_{ax} was kept constant at 5 mm. This axial gap width was chosen due to the results of previous experiments [21] on the influence of the axial gap width s_{ax} between flat-disk-shaped back shroud and rear housing wall on fiber entry into the back shroud cavity of the same wastewater pump. The tests with axial gap widths s_{ax} of 1, 2, 3, 4 and 5 mm showed a general decrease in fiber entry with the decrease in axial gap width. In order to assess the effectiveness of the recess configurations presented in this paper, it was decided to select the maximum gap width as a reference, at which the chance of fiber entry is high. Radial gap width s_r as well as degree of back shroud coverage c_{BS} were varied throughout the tests. Table 6 provides an overview over the investigated housing recess geometries. Several of these configurations as well as the reference configuration UBS5 are illustrated in Figure 27. The given designations correspond to the type of modification, the back shroud coverage c_{BS} and the radial gap width s_r. In order to easily compare the housing recess geometries presented with those in other pumps, it is also useful to specify the radial gap ratio as follows:

$$S_r = \frac{s_r}{R_{BS}} \tag{8}$$

The various configurations were implemented by screwing 3D-printed polylactide rings onto the acrylic glass back wall, as shown for configuration HR 100.8 in Figure 28.

Table 6. Housing recess configurations.

Designation	c_{BS} [-]	s_r [mm]	S_r [-]
HR 0.8	0	8	0.0578
HR 50.8	0.5	8	0.0578
HR 100.8	1	8	0.0578
HR 0.2	0	2	0.0144
HR 50.2	0.5	2	0.0144
HR 100.2	1	2	0.0144



(**a**) UBS5 (**b**) HR 0.8 (**c**) HR 50.8 (**d**) HR 100.2

Figure 27. Selected configurations in comparison.

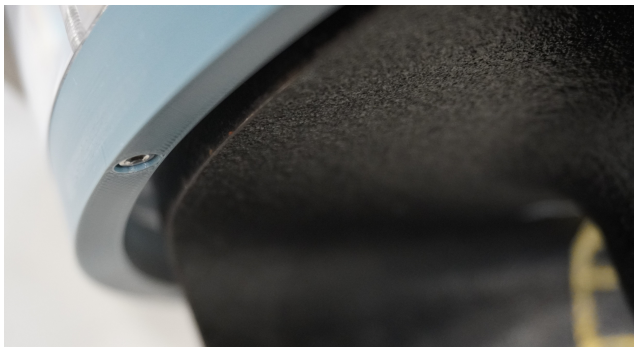


Figure 28. Radial gap of housing recess configuration HR 100.8.

Test Procedure

For each configuration, three different operating points were investigated, one at part load (Q50), one at the best efficiency point (Q100) and one at overload (Q120). For a corresponding configuration, three tests were performed per operating point. Each configuration was evaluated regarding the permanent dry fiber mass entry into the back shroud cavity after a test duration of 60 min after completion of the ramp-up process.

Prior to each test, the flow rate of interest was adjusted using the regulation valve. Reference values for head and electrical power were then obtained under clear-water conditions. The reference values are needed to monitor the operating behavior throughout each test, as well as to determine any geometry-induced influence on both operating behavior and overall efficiency. The latter is obtained as follows:

$$\eta_o = \frac{P_{hydr}}{P_{el}} = \frac{\rho \cdot g \cdot Q \cdot H}{P_{el}} \tag{9}$$

At the end of each test, the pump was switched off, and the test rig was drained into a filtration system, where the fiber-laden water was prepared for the next test. The bearing bracket and the impeller were then removed. After taking the impeller off the shaft, possible fiber accumulations were collected and subsequently dried in a dehydrator until no more evaporation-induced weight loss was detectable. Table 7 provides an overview of the uncertainties of the measurement methods used.

Table 7. Measurement uncertainties.

Quantity	Uncertainty
flow rate	±0.2% of value
differential pressure	±0.05 bar
electrical power	±1% of value
mass	±0.005 g

4.4. Results

The configurations listed in Table 6 are evaluated below on the basis of the dry fiber mass entry into the back shroud cavity. Results for the reference configuration of equal back shroud geometry without housing recess *UBS5* obtained in [21] are used as a reference. In Figures 29 and 31, the markers, upper bars and lower bars represent the mean, maximum and minimum values of dry fiber mass entry, respectively.

4.4.1. Radial Gap Width s_r of 8 mm

Figure 29 shows the results for the housing recess geometries with a radial gap width s_r of 8 mm. At part load Q50, no fiber entry into the back shroud cavity was detected for all configurations investigated.

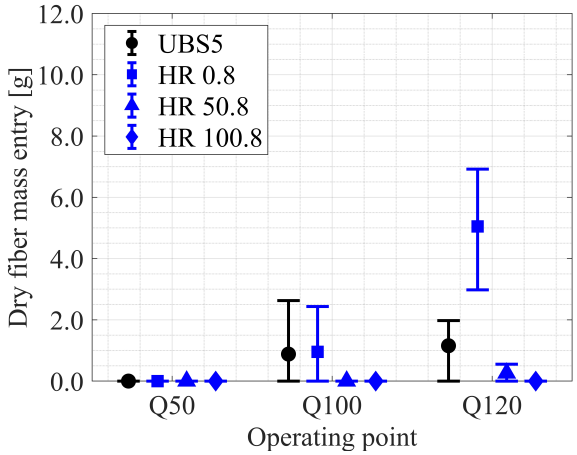
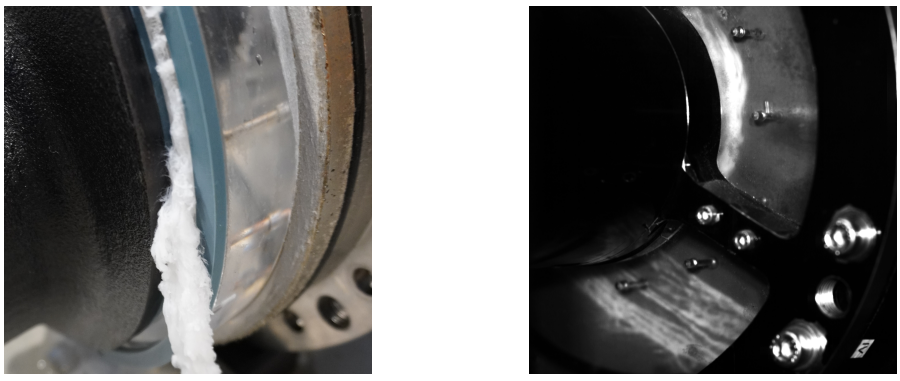


Figure 29. Dry fiber mass entry at s_r of 8 mm.

At the best efficiency point, Q100, however, significant fiber entry into the back shroud cavity took place when testing configuration HR 0.8, as shown in Figure 30a. For this configuration, which fully covers the back shroud cavity but not the back shroud, fiber entry was quantitatively very similar to that of the recess-free reference configuration UBS5. In contrast, configurations HR 50.8 and HR 100.8 showed no fiber entry at the best efficiency point, effectively reducing fiber entry into the back shroud cavity.

At Q120 overload operation, fiber entry was distinctly increased by configuration HR 0.8. Compared with configuration UBS5, mean fiber entry more than quadrupled. As shown in Figure 30b, once more, fibers were observed to jam the passage to the back shroud cavity. In addition, fibers wound up on the rotating hub. With a partial back shroud coverage c_{BS} of 0.5, in contrast, fiber entry was significantly reduced, as the mean value of 0.26 g corresponds to 22.5% of the fiber entry registered for configuration UBS5 at this operating point. Configuration HR 100.8, due to its full back shroud coverage, eliminated fiber entry at Q120 overload operation.



(**a**) best efficiency point (**b**) overload

Figure 30. Fiber accumulations observed when operating configuration HR 0.8.

4.4.2. Radial Gap Width s_r of 2 mm

For the housing recess geometries with a smaller radial gap width s_r of 2 mm, the operating point-dependent dry fiber mass entry is shown in Figure 31.

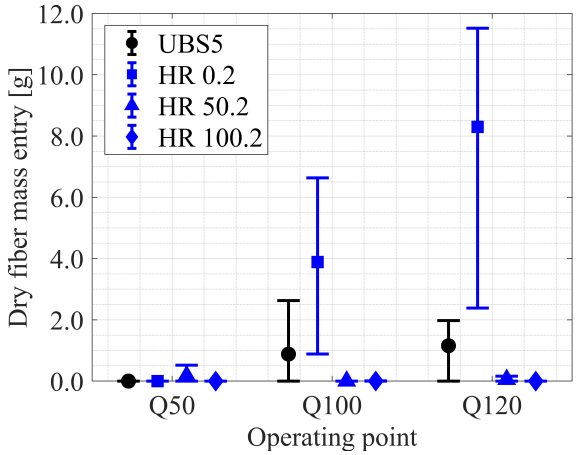
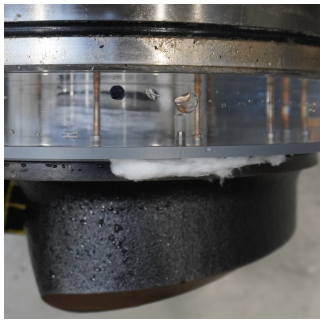


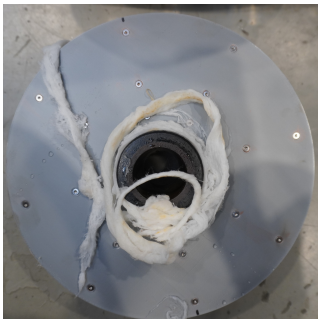
Figure 31. Dry fiber mass entry at s_r of 2 mm.

With the exception of configuration HR 50.2, none of the configurations examined at Q50 part load showed any significant fiber entry into the back shroud cavity. This is remarkable, since significant fiber entry into the back shroud cavity proved to be rare for the investigated pump at part load. However, two of the three tests carried out with configuration HR 50.2 at part load were free of any fiber entry.

At the best efficiency point, Q100, HR 0.2 was found to be the only housing recess configuration with significant fiber entry into the back shroud cavity. In Figure 32a, fibers jammed in the passage to the back shroud cavity can be seen. Figure 32b shows the massive amount of fibers wound up on the hub after the same test at the best efficiency point with a dry mass fiber entry of more than 6.6 g.



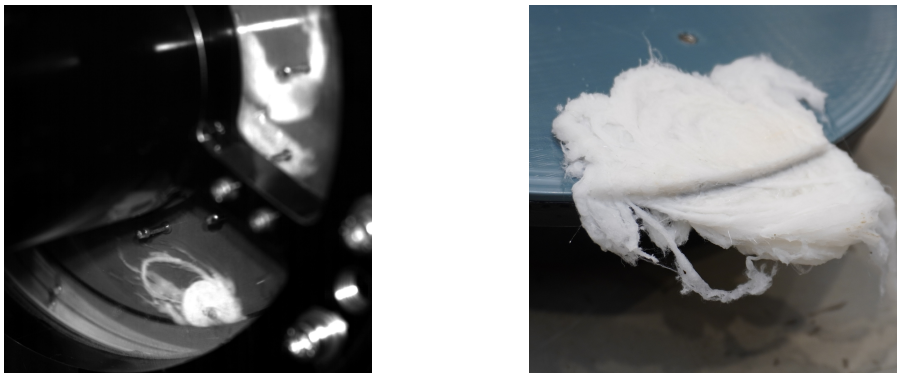
(**a**) jammed fibers



(**b**) wound up fibers

Figure 32. Fiber accumulations after operating configuration HR 0.2 at the best efficiency point.

When operating the housing recess configurations with a radial gap width s_r of 2 mm at Q120 overload, strongly increased fiber entry was detected for HR 0.2 once more. With a maximum value of 11.52 g for this configuration at this operating point, the largest dry fiber mass entry of the entire test series was determined. Again, fibers were seen to both wind up on the rotating hub and jam the passage to the back shroud cavity, as shown in Figure 33a. As can be further seen in Figure 33b, fiber entry was so severe that the back shroud and recess geometry were damaged and had to be replaced. With a value of 0.16 g, maximum dry fiber mass entry was much less due to increased back shroud coverage c_{BS} but still considerable when operating housing recess configuration HR 0.5 at overload. It was again the configuration with the maximum back shroud coverage c_{BS} that showed no fiber entry at overload.

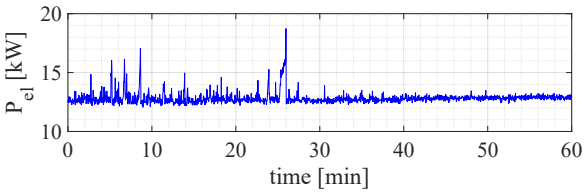


(**a**) during operation (**b**) after operation

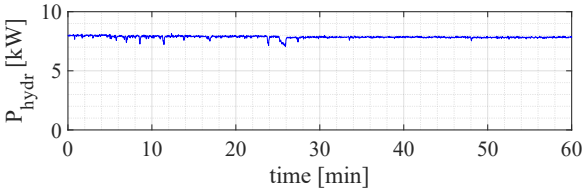
Figure 33. Configuration HR 0.2 at overload.

4.4.3. Influence on Performance

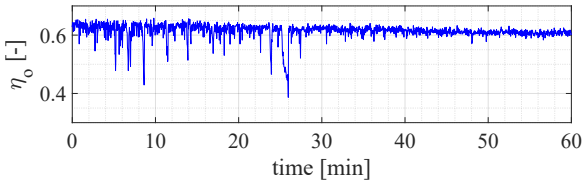
In Figure 34 it can be seen that fibers jamming the passage to the back shroud cavity were particularly evident when examining the recorded performance data, including electric power input P_{el}, hydraulic power output P_{hydr} as well as the resulting overall efficiency η_o. Reference values P_{el} and P_{hydr} obtained prior to this test corresponded to 12.45 kW and 8.06 kW, respectively. As can be seen in Figure 34a,b, P_{el} increased to 12.89 kW by the end of the test due to the frictional torque caused by the jammed fibers, while P_{hydr} was reduced to 7.84 kW. Figure 34c shows that overall efficiency η_o was thus significantly reduced from 0.648 to 0.609. This influence on the performance data could only be determined for the strong jamming of fibers accumulated in the passage to the back shroud cavity. In the case of minor fiber accumulations of this type and fibers wound up on the hub or the shaft, no such influence on the operating behavior was determined.



(**a**) electric power



(**b**) hydraulic power



(**c**) overall efficiency

Figure 34. Performance data for configuration HR 0.2 at overload.

4.4.4. Clearwater Efficiency Comparison

Measures to increase functionality are also to be evaluated on the basis of their influence on efficiency. Improving the clogging behavior of a wastewater pump often goes together with a reduction in efficiency. Figure 35 shows the overall efficiency η_o averaged over the three operating points for all housing recess configurations investigated as well as the recess-free reference configuration UBS5. It can be seen that the overall efficiency η_o for the introduced housing recess configurations is generally equal or higher compared with configuration UBS5. Furthermore, overall efficiency proved to increase with the increase in the degree of back shroud coverage c_{BS} and the decrease in radial gap width s_r.

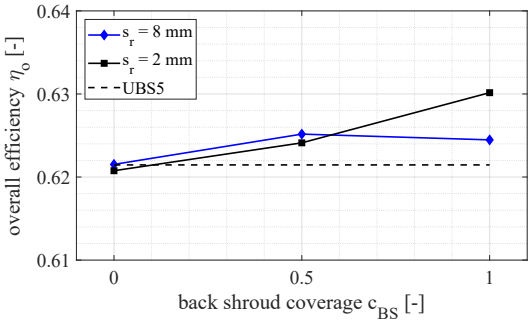


Figure 35. Operating point-averaged overall efficiency.

4.5. Discussion

For the investigated pump and range of the parameters back shroud coverage c_{BS} and radial gap width s_r, the presented results lead to the finding that to prevent fiber entry into the back shroud cavity by decoupling back shroud cavity and housing using a suitable recess geometry, high back shroud coverage c_{BS} is to be preferred over small radial gap width s_r. This deduction is based on the fact that for all radial gap widths s_r investigated, the increase to moderate and to complete back shroud coverage c_{BS} generally led to a significant reduction in and complete elimination of fiber entry, respectively. In contrast, for configurations with insufficient back shroud coverage c_{BS}, an increase in fiber entry with the decrease in radial gap width s_r was evident.

As discussed in Section 4.1.3, decoupling the back shroud cavity flow from the flow in the housing was expected to decrease fiber entry into the back shroud cavity. It was further elaborated that the extent to which these flows are decoupled generally increases with the increase in back shroud coverage c_{BS} and the decrease in radial gap width s_r. These expectations have only proven to be valid for housing recess configurations in which the decoupling of the back shroud cavity flow was pursued by sufficiently large back shroud coverage c_{BS} and radial gap widths s_r that are not too small. However, this does not directly contradict the literature from which the expectations were derived, as the findings stated therein refer to clear-water conditions without fibers or other solids. With only 2 mm, the minimum radial gap width s_r selected in this work may provide a significant decoupling of the back shroud cavity from external boundary conditions under clear-water conditions. Despite this, however, this proved to result in an unfavorable passage to the back shroud cavity, which causes fiber accumulations to get jammed and prevents them from easily exiting the back shroud cavity.

In cases of severe jamming, electrical power input P_{el} was observed to increase, whereas hydraulic power output P_{hydr} was determined to decrease, thus decreasing overall efficiency η_o. In the case of minor jamming or fibers wound up on the hub or the shaft, no such influence was detected. Compared with the recess-free reference configuration, clear-water overall efficiency η_o of the housing recess configurations presented was equal or higher by up to nearly 0.01.

5. Transient Instationarities of Mechanical Load and Discharge Pressure in Wastewater Pump Operation

With Section 2 optimizing the sedimentation behavior in a round wastewater pumping station in order to ensure the transport of solids in wastewater through the pumps and Sections 3 and 4 optimizing the impeller and housing of such pumps in order to reduce their susceptibility to clogging, this section concerns the implications of clogging in wastewater pumps. In particular, the transient instationarities in the mechanical load induced by clogging are dissected and analyzed in detail.

5.1. Materials and Methods

5.1.1. Test Rig Setup and Tested Pumps

The test rig and test procedure employed for the analysis of transient instationarities in the mechanical load and discharge pressure of a wastewater pump are the same as already detailed in Section 3.1.2. For the purposes of the subsequent analyses, all parameters are simultaneously and synchronously measured at a higher sampling frequency of 1 kHz. This enables the analysis of the torque in the frequency domain while being able to synchronously consider all other parameters.

The pumps subjected to the subsequent methodology and analyses have already been presented in detail in Section 3.1.1. The modifications of the optimized impeller MOD 0, MOD 1, and MOD 2 are considered in the following analysis of torque transients. For all impellers, a clear-water reference measurement of 30 s is recorded as a frame of reference for the functional performance tests. For MOD 0, only the smallest (L25) contamination class is tested due to the high susceptibility to clogging. For MOD 1 and MOD 2, tests with the smallest (L25) and intermediate (L50) contamination classes are performed.

5.1.2. Frequency-Domain Transfer

Fourier transform. The frequency-domain transfer is set up in a similar fashion to the work by Brokhausen et al. [29]. The process will also be briefly described here.

The frequency-domain transfer is executed via a discrete Fourier transform (DFT) since the data it is applied to are characterized as real-valued and digitized. The result of this transform is a complex amplitude spectrum over the frequencies. These complex amplitudes are converted into real, absolute values and are converted back into their original value domain for ease of interpretation. This is implemented as follows (adapted from [48] (p. 61)):

$$\hat{A}_p = \frac{2 \cdot |\hat{A}_{complex}|}{N}, \tag{10}$$

where A_p are the peak amplitudes in the original value domain, $A_{complex}$ are the complex amplitudes, and N is the number of data points that the DFT was applied to. These amplitude values represent the peak values of the oscillation and are subsequently converted into their root mean square (RMS) values as follows [48]:

$$\hat{A}_{rms} = \frac{\hat{A}_p}{\sqrt{2}}, \tag{11}$$

Windowed DFT. The frequency transform is applied in a windowed fashion. The window is shifted by a certain number of samples across the data, where a DFT is carried out per window. This enables the resolution of the amplitudes over time. The number of samples that the window is shifted by, therefore, defines the resolution in time. The frequency resolution is defined by the size of the window. The smallest frequency that can be resolved is determined by the division of the sampling frequency by the window size.

The extracted windows of data need to be further conditioned. When extracting a subsection of data, the constituent waveforms are cut at a point that is unequal to their period. This leads to the detection of amplitudes for frequencies, which in reality do not exist in the data. This phenomenon is called spectral leakage. It is countered by applying a window function to each window. In this study, the Hamming window is used. The Hamming window represents a bell curve with reduced kurtosis and is formulated as follows [49]:

$$w(n) = 0.54 - 0.46 \cdot \cos\left(\frac{2\pi n}{N-1}\right), \quad with\ 0 \leqq n \leqq N-1 \tag{12}$$

where N represents the number of samples in a window. The window function essentially dampens the edges of the windows to reduce their influence in terms of spectral leakage. With the application of this function, however, the resulting amplitudes of the DFT are of course altered. In order to counter this and be able to still interpret the amplitude spectrum in the original value domain, an amplitude correction factor needs to be applied. The correction factor is calculated by Equation (13) [50] (p. 212):

$$CF = \frac{N}{\sum_{n=0}^{N-1} w(n)}, \tag{13}$$

where, again, N is the size of the window. The resulting amplitudes are all multiplied by this correction factor.

Implementation details. The frequency-domain transfer via the windowed discrete Fourier transform is executed with a window size of 2000 samples. As mentioned, the sampling frequency of the torque measurement is 1000 Hz, making the window two seconds long. Moreover, this results in a frequency resolution of 0.5 Hz. This is a sufficient resolution in frequency as the frequencies of interest are not as close to one another as to necessitate a finer sub-Hertz resolution. This is demonstrated in the subsequent chapter.

With this setup, the maximum frequency that can be identified is 500 Hz, which is far enough for the harmonics being observed in the measurements, as demonstrated later on in the Results Section. Lastly, the number of samples the window is shifted by is set to 1000, i.e., 1 s. This ensures a sufficient resolution in time.

5.1.3. Definition of Harmonics

The reason for the frequency-domain analysis is to be able to identify and trace harmonics in the torque signal. The expected and observed harmonics originate due to the inherent periodic nature of the mechanic rotation. Therefore, the main base frequency is the rotational frequency (RF). One specific additional frequency of interest is the so-called blade passing frequency (BPF), i.e., the frequency with which the blades of the pump's impeller rotate. Naturally, this depends on the number of blades and manifests as the product of the latter and the rotational frequency. As all pumps in this study employ two-channel impellers, i.e., possessing two distinct blades, their blade passing frequency is twice the rotational frequency.

The notion of harmonics manifests as integer multiples of these base frequencies. Table 8 shows the frequencies of interest evaluated in this study. The table shows both the exact frequency and the binned frequency at which the respective harmonic will be identified due to the frequency resolution of 0.5 Hz.

Table 8. Non-exhaustive list of frequencies of interest.

Description	Exact Value	Binned Value
Rotational Frequency (RF)	$24.1\overline{6}$ Hz	24 Hz
Third Harmonic of RF	72.5 Hz	72.5 Hz
Fifth Harmonic of RF	$120.8\overline{3}$ Hz	121 Hz
Seventh Harmonic of RF	$169.1\overline{6}$ Hz	169 Hz
Blade Passing Frequency (BPF)	$48.\overline{3}$ Hz	48.5 Hz
Second Harmonic of BPF	$96.\overline{6}$ Hz	96.5 Hz
Third Harmonic of BPF	145 Hz	145 Hz
Fourth Harmonic of BPF	$193.\overline{3}$ Hz	193.5 Hz

The table shows another important peculiarity. In this case, the second harmonic of the rotational frequency is synonymous with the blade passing frequency, as both manifest at twice the rotational frequency. Therefore, only the odd harmonics of the rotational frequency are regarded.

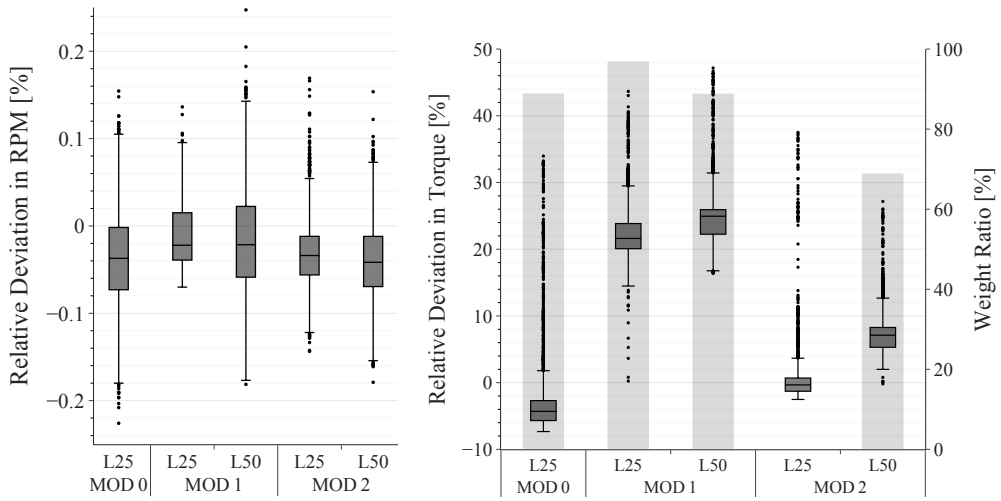
Additionally, as some of the actual frequencies fall in between the binned frequencies due to the noted frequency resolution and due to instationarities in the operation, the frequency bin that the harmonic manifests in can change. In order to account for cases like this and general variance in the exact occurrence of the harmonic amplitude peaks, these are identified as the most prominent peak within a range of ± 5 Hz around the theoretically defined center frequency.

In the remainder of this section, these harmonics may be referred to with a shortened descriptor in the format of $(X\cdot)RF$ and $(X\cdot)BPF$ to represent the X^{th} harmonic.

5.2. Results

5.2.1. Analysis in Value Domain

Figure 36 shows the distributions of the relative deviation in the rotational speed in rotations per minute (RPM) and torque in relation to the recorded clear-water reference.



(**a**) rotational speed (**b**) torque

Figure 36. Box plots for all tests showing the distribution of the relative deviation in respect of clear-water operating points. Plot (**b**) additionally shows the weight ratio as bars mapped to the second, right-sided y-axis.

For the analysis of the distribution of values of the rotational speed, the normalized, relative values are shown as individual box plots per test in Figure 36a. These values can

be interpreted as a percentage-wise increase or decrease in rotational speed compared with the set rotational speed recorded under clear-water operating conditions. The x-axis shows the labels for the respective pump as well as the contamination class employed in the test.

As can be seen by the very small range of the y-axis, the rotational speed varies very little during the long-time functional performance test with artificial wastewater. The largest deviation from the set rotational speed within the tests is only ±0.25%. The median rotational speed of all tests even falls within ±0.05% of the set speed.

The distribution of assumed torque values during the tests is represented in the same way as the rotational speed in Figure 36b. This figure additionally shows the weight ratio of each test as a bar, mapped to the right-sided y-axis. The weight ratio signifies the amount of dusters that are accumulated inside the pump at the end of the respective test.

In contrast to the rotational speed, the torque shows a lot more variation, with maximum deviations exceeding a 40% increase in the needed torque compared with clear-water operation. Further, many more outliers can be observed, as seen by the number of markers beyond the whiskers of the box plots. This represents the occurrence of sudden spikes and peaks in the torque induced by the dusters' interference with the impeller.

The overlayed weight ratio shows the relation between the severity of clogging of the pump and the attributed deviation in the necessary torque. For MOD 0, almost 90% of the introduced dusters are clogged inside the pump after the test. The torque, however, shows a median decrease of 4%. The clogging of the impeller, shown in Figure 19 to be blocking the channels of the impeller, subsequently leads to a reduction in the needed torque. However, there are also many outliers to be seen where the torque increased up to 34%. This will be regarded in more detail in the integrated time- and frequency-domain analysis.

For MOD 1 the median torque for both functional performance tests with contamination classes L25 and L50 increases by 22 and 25%, respectively. The outliers also exhibit higher values than for MOD 0 with the largest increases among all regarded tests of up to 48%. The weight ratio of the clogging inside the pump impeller is also slightly higher for MOD 1 than for MOD 0.

Lastly, the tests for MOD 2 exhibit significantly less deviations in torque. For the test with the lowest contamination class, the median deviation in torque is close to zero, and 50% of the test time, the torque falls within ±1% of the respective clear-water operation, as signified by the first and third quartiles. This is in line with the fact that for this test, no clogging was observed inside the impeller at the end of the test. The outliers shown in the distribution might hint at short-lived and volatile clogging phenomena, which will be examined in the later integrated time- and frequency-domain analyses. Lastly, the test of MOD 2 with the intermediate contamination class exhibits a median increase of about 7% in torque, with outliers reaching an increase of up to 27%. With a weight ratio of about 70%, the clogged weight is still quite large but less than exhibited for MOD 0 and MOD 1.

Discussion. The analysis of the rotational speed shows how well the VFD regulates and controls the delivered speed. Despite the demonstrated variations in torque, the set rotational speed can be very accurately maintained by the control.

The deviations in the operating conditions present due to the clogging of the pump are mechanically only reflected in the supplied torque. However, this effect of clogging on the relative deviation of the torque is not consistent. Test MOD 0-L25 shows a large weight ratio of dusters clogged in the pump but, for the most part, similar of slightly smaller levels of torque than in clear-water operation, while tests MOD 1-L25, MOD 1-L50, and MOD 2-L25 exhibit large weight ratios and increased torque levels. Therefore, no uniform, generalized statement regarding the torque deviation when clogging occurs can be made on the basis of the underlying test data.

However, test MOD 2-L25 serves as an example for a clogging-free impeller, for which no persistent deviation in torque can be observed.

5.2.2. Analysis in Frequency Domain

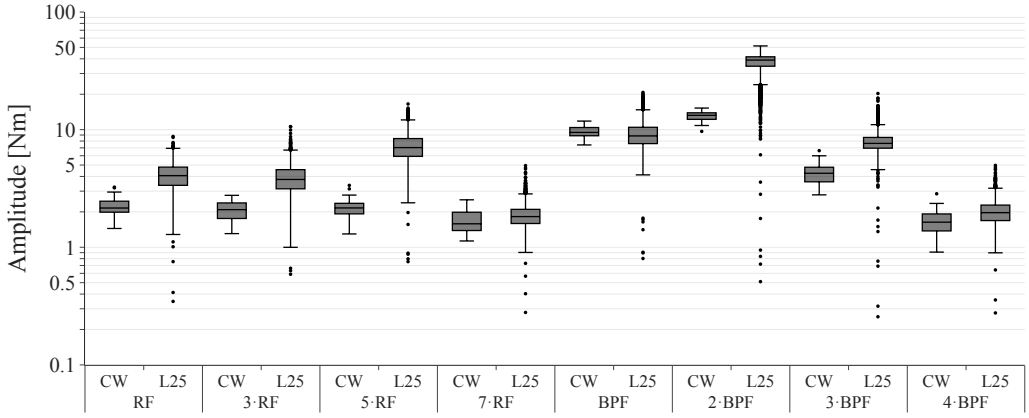
After the analysis of the rotational speed and the deviations in torque in the value domain, the torque is analyzed in the frequency domain. The frequency-domain transfer and analysis scheme of the harmonic frequencies are detailed in Section 5.1.2. For this analysis, Figure 37 shows the amplitudes of selected harmonic frequencies. The leveraged harmonic frequencies are the rotational frequency (RF) and its third, fifth, and seventh harmonic, as well as the blade passing frequency and its second, third, and fourth harmonics. Higher-order harmonics are not examined in detail, as the absolute amplitude values for clear-water measurements as well as the amplitudes for the functional performance tests flatten out towards higher-order harmonics and become indistinguishable from the general noise in the amplitude spectra. The individual graphs shown integrate the distribution of amplitude values for the clear-water reference, denoted by CW, as well as for each functional performance test, denoted by the corresponding employed contamination class L25 or L50. The scaling on the ordinate is chosen to be logarithmic in order to be able to interpret the amplitude values despite the partially vastly different magnitudes.

In Figure 37a, the amplitude for the CW measurement and the test with 25 dusters per cubic meter are shown side by side. Regarding the amplitudes of the RF, 3·RF, and 5·RF, there are noticeable increases in the distribution of amplitude to be observed, as all first quartiles of the amplitude distributions for the functional performance tests exceed the third quartiles of the CW reference. The median increases are 2 Nm for the RF and 3·RF and 5 Nm for the 5·RF. For the 7·RF, the previously described reduction in amplitude for the CW and FPT can already be observed with values mostly below 2 Nm. The BPF and 2·BPF exhibit higher median amplitudes for both CW and FPT than any other harmonic for MOD 0. However, the amplitudes for the BPF do not differ a lot between CW and FPT. For the 2·BPF, a median increase from 13 to 42 Nm can be observed, showcasing the largest increase for this modification. The amplitudes for the 3·BPF also exhibit an increase, while the 4·BPF amplitudes already manifest the tendency of inconspicuous behavior for higher-order harmonics.

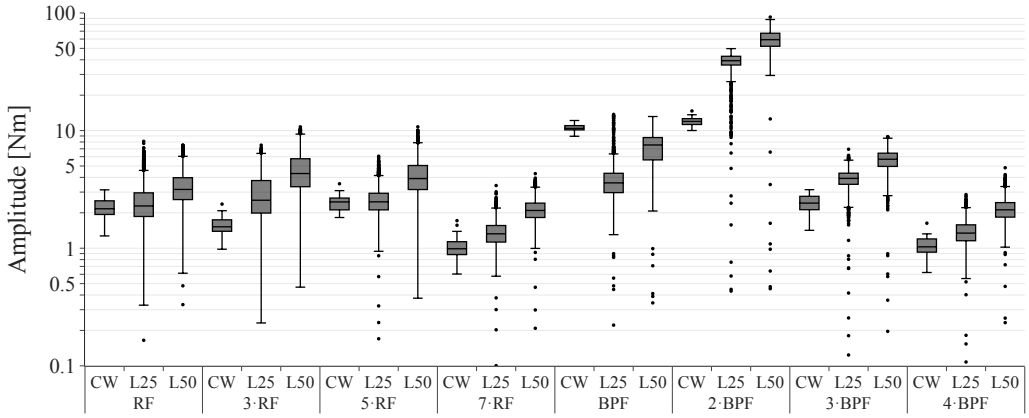
Figure 37b shows the results for the CW measurement as well as the FPT with contamination classes L25 and L50 for impeller MOD 1. The analysis of the RF and its harmonics reveals similar tendencies to those observed with MOD 0. There are small but noticeable increases in the amplitudes of the RF, 3·RF, 5·RF, and 7·RF, while the latter exhibits the smallest values overall. Interestingly, the amplitudes also show a clear trend to increase with an increase in the contamination class; i.e., the interactions of the dusters with the impeller and the increased clogging of the impeller lead to increased amplitudes for the RF and its harmonics. The amplitudes of the BPF show a different behavior, with the amplitudes for the FPTs actually decreasing. The test with contamination class L25 exhibits a median drop in amplitude of 7 Nm. The amplitudes of the harmonics of the BPF again exhibit the trend to increase with higher contamination classes. For the 2·BPF, the median increases by 30 and 50 Nm, respectively, for the FPTs with L25 and L50. The latter test exhibits the overall highest observed amplitude for the 2·BPF with up to 92 Nm.

Finally, Figure 37c shows the distributions of amplitudes for MOD 2. When comparing the amplitudes of the CW measurement and the FPT with contamination class L25, there are only minor differences to be seen in the outliers of the FPT. In this test, there was no clogging inside the impeller at the end of the test, signifying that the interaction of dusters and impeller, without prevailing clogging, seems to only minorly influence torque oscillation in terms of harmonic amplitudes. The FPT with contamination class L50 exhibits more

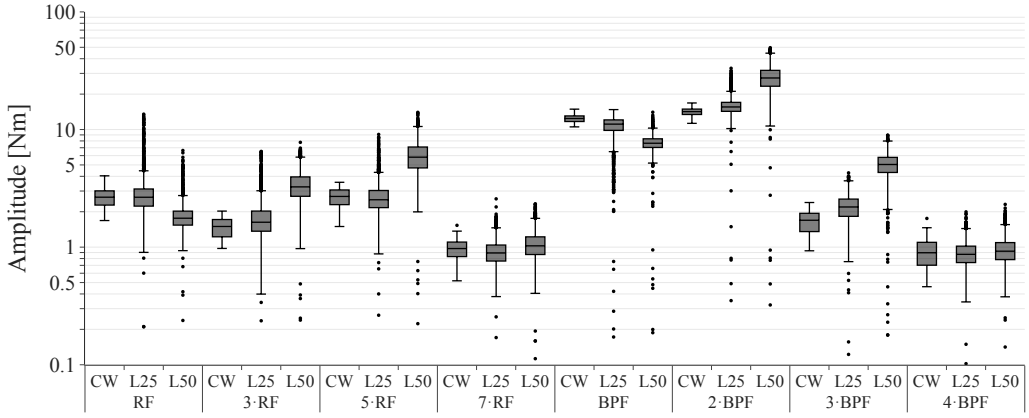
influence on the amplitudes due to the prevailing clogging of the impeller. The tendencies of respectively increasing and decreasing amplitudes for the individual harmonics follow the previously explored patterns—with one exception: regarding the amplitudes of the RF, peculiarly, the amplitude decreases due to clogging within test L50.



(**a**) MOD 0



(**b**) MOD 1



(**c**) MOD 2

Figure 37. Amplitudes for selected harmonics of the rotational frequency (RF) and blade passing frequency (BPF) for clear-water reference measurements (CW), and functional performance tests with contamination classes L25 and L50, where applicable, for the three modifications of the presented impellers.

Discussion. The detailed analysis of the amplitudes of harmonic frequencies in the torque of the wastewater pumps under test demonstrates the high variance in harmonic content induced by the operation in artificial wastewater. It is shown that the amplitudes for most harmonics tend to increase due to the interaction of dusters with the impeller as well as prevailing clogging. These implications lead to partially drastic amplitudes, as the maximum value of almost 92 Nm for just the 2·BPF in test MOD 1-L50 demonstrates. Considering that these amplitudes are formulated as RMS values of the underlying oscillation, the actual peak amplitude of the torque that the whole system is exposed to is even higher. Further, all shown frequencies naturally overlap and amount to a high-stress situation.

The optimization of impeller MOD 2 as introduced in the paragraph *Impeller Variation* in Section 3.1.1 not only leads to the clogging-free behavior in test L25 but also to very little influence observed in the harmonic content of torque in this test.

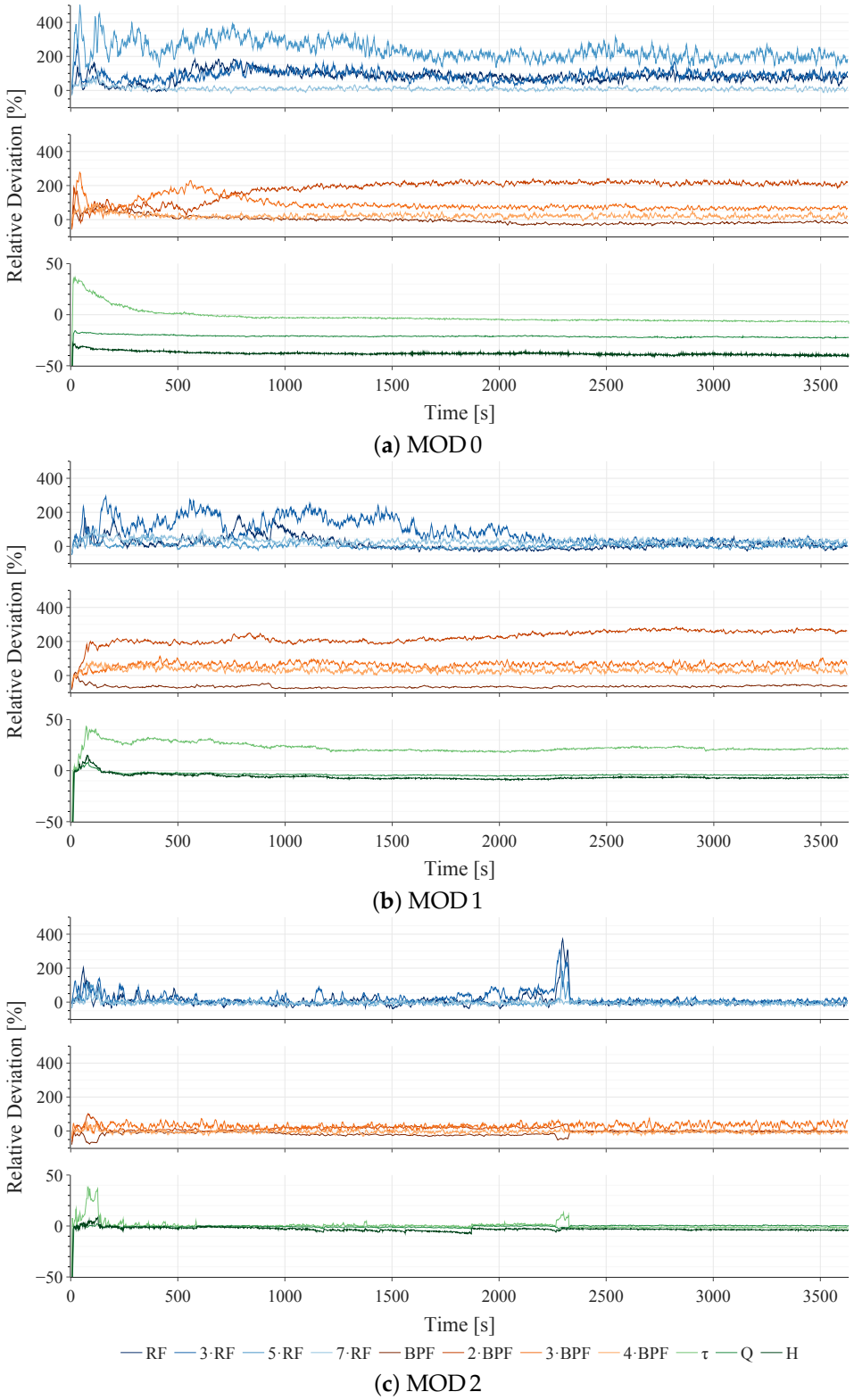
5.2.3. Integrated Time- and Frequency-Domain Analysis

After observing the relative and absolute changes in rotational speed, torque and oscillation in torque in terms of salient harmonics, these parameters are regarded jointly in the time domain. As all measurements from the test rig are synchronized, the following graphs in Figure 38 not only show the detailed analysis of torque and its harmonics but also flow Q and head H in order to judge the influence of clogging on hydraulic performance. Therefore, each of the individual graphs shows the relative deviation in flow, head, and torque in the respective bottom plot, the relative deviation in amplitude for the blade passing frequency and its harmonics in the middle plot, and the same for the rotational frequency and its harmonics in the respective top plot. The reported data stem from the functional performance tests with the same contamination class, L25, for all three modifications of the impeller.

Figure 38a shows the graph for MOD 0. The bottom plot shows that from the start to the end of the test, the flow and head of the pump drop by 20 and 40%, respectively. These values do not show any variation over the course of the test. The relative deviation in torque peaks at the beginning at an increase just under 40% , then drops to its initial clear-water reference value, and slowly decreases over the remainder of the test duration to a final value of about −7%. These parameters signify that there is extensive, persistent clogging of the impeller. The amplitudes of the harmonics of the BPF in the middle plot show heightened levels throughout, with the 2·BPF increase reaching a plateau at around 225% and the 3·BPF increase at around 75%. The harmonics 2·BPF and 3·BPF also exhibit initial deviations from their stagnant plateaus coinciding with the initial spike and drop in torque. The BPF itself and the 4·BPF show inconspicuous levels, with only slightly respectively increasing and decreasing amplitudes towards the end of the test of around ±25%. The RF and its harmonics in the top plot also partially exhibit increased levels, with the RF and 3·RF increases leveling out at around 75%, while the 5·RF increases up to around 200%. For the latter, in the beginning there are spikes in amplitude reaching values of just under 500%.

For the test of MOD 1 in Figure 38b, the flow and head show only small deviations for the majority of the test, decreasing by about 5 and 7.5% respectively. The torque stagnates at an increase of about 20%. Only in the beginning of the test, between the 30 and 130 s marks, there are increased levels of flow and head and even larger increases in torque. The torque level slowly drops from 40% to the final 20% increase over a duration of about 1000 s. In this time frame, the amplitudes of the RF and 3·RF also show lots of variation, with an increase in amplitude of the latter of up to 300%. The amplitudes of the RF and its harmonics reduce towards the end of the test and fluctuate between a −25% decrease and a 50% increase. The amplitudes of the BPF are lower than their clear-water reference

with decreases of around 75%. The 3·BPF and 4·BPF increases level out at 50 to 75% and the 2·BPF increase at around 270%.



(**a**) MOD 0

(**b**) MOD 1

(**c**) MOD 2

Figure 38. Relative changes in amplitude for selected harmonics of the rotational frequency (RF) and blade passing frequency (BPF) over time, synchronized with flow, head and torque measurements for the functional performance tests with contamination class L25, for the three modifications of the presented impellers.

Lastly, the reported test for MOD 2, reported in Figure 38c, shows rather inconspicuous harmonic levels most of the time. The same holds true for the hydraulic metrics and the overall torque level. However, there are two distinct events, at the beginning of the test and between 2250 and 2350 s, where the torque values increase drastically for a short duration. These events are also reflected in the harmonics, where for both events, the amplitude of the BPF drops below its clear-water levels. For the vast majority of the test, all amplitude levels of the RF and its harmonics are close to 0%, as are the BPF and its harmonics. Solely the 3·BPF increase shows slightly heightened levels of around 40%.

Discussion. The integrated analysis of the time- and frequency-domain metrics underlines the previously established conclusions. The clogging of the impeller of a pumps leads to string fluctuations in amplitude in several harmonic frequencies. The increases in amplitude amount to up to 500%, with actual peak amplitude values beyond 100 Nm. The shown traces of harmonic amplitudes, synchronized with hydraulic measurements, demonstrate the importance of optimizing impellers for wastewater applications. Not only does the general performance increase with low susceptibility to clogging, but also the high-frequency, high-amplitude fluctuation in torque is reduced, thereby reducing the stress induced on the whole system. The test for MOD 2 with contamination class L25 is exemplary for this, as the optimized impeller does not show persistent clogging events with overall small fluctuations in torque.

6. Conclusions

This paper presents several examples of challenges and possible optimization approaches for the operation of pressurized sewerage systems. The analysis begins with a look at the entire pumping station. A physical model configured using hydraulic scaling is used as an optimization tool. The solids contained in wastewater can be represented in a scaled model using plastic granulate. This approach shows how specific insights into sedimentation patterns in suction chambers can be gained. Based on modifications aimed at improving the geometry of the suction chamber with regard to sedimentation susceptibility, a significant reduction in particle retention is achieved. Further considerations also relate to the inlet and outlet positions and the flushing intervals. With the help of the optimized suction chamber design, wastewater can be transported to the pump with minimal sedimentation.

In order to leverage the potential of optimized suction chambers in pressurized sewerage systems, low-clogging pumps are essential. The presented methodology for designing efficient wastewater impellers using 3D-CFD combined with response surface optimization shows that wastewater impellers with high efficiency within the estimated ranges can be developed. However, the long-time functional performance tests reveal a trade-off between functionality and efficiency. The efficiency-optimized impeller shows insufficient functionality due to its thin, flow-optimized leading edges. By adjusting the geometry of the leading edges, in particular by using cut-back and thickened leading edges in combination with a lowered impeller screw, significant improvements in slip behavior are observed in the optical investigations, resulting in increased functionality for the functionality-optimized impeller with a moderate reduction in efficiency of approximately 5% relative to the efficiency-optimized impeller.

Further optimization of the pump itself concerns the potential influences of housing recesses on the back shroud cavity flow and the resulting fiber entry. To determine the respective influence of the relevant parameters of back shroud coverage and radial gap width, suitable back shroud cavity configurations with housing recesses are designed. The corresponding configurations are experimentally investigated and evaluated on the basis of dry fiber mass permanently accumulated in the back shroud cavity after pumping artificial

wastewater for 60 min. The conducted experiments lead to the finding that fiber entry into the back shroud cavity is significantly reduced or completely eliminated as the back shroud coverage is increased. In contrast, an increase in fiber entry is determined when reducing the radial gap width for configurations with insufficient back shroud coverage. In this configuration, fibers are frequently observed to jam the passage to the back shroud cavity, reducing overall efficiency in severe cases. Fibers are also exhibited to wind up on the hub or the shaft. However, a related significant influence of this phenomenon on pump performance is not detected. The investigated housing recess geometries show equal and, in case of partial or full back shroud coverage, increased overall efficiency. However, further knowledge about the prevailing flow within the back shroud cavity is to be determined numerically or experimentally. Since the presented results are limited to the investigated wastewater pump, it is of further interest to find out whether the findings also apply to other pumps.

The last part of this holistic analysis of wastewater pumping stations presents insights into the clogging-induced instationarities of torque demonstrated in standardized long-time functional performance tests on efficiency- and functionality-optimized semi-open two-channel impellers. The transient instationarities are demonstrated in the frequency domain of the torque signal as amplitudes of harmonic frequencies which are regarded synchronously to torque, head and flow in the value domain. In particular, the clogging of the impeller was shown to lead to increased required torque levels as well as large increases in torque oscillation. The latter manifests as amplitude increases of the rotational and blade passing frequencies with transient, relative increases of up to almost 500%. In contrast, it is demonstrated that the optimization of the impeller for functionality with the aim to reduce its susceptibility to clogging also leads to drastically reduced torque oscillations which can be mostly indistinguishable to clear-water operation.

Apart from the optimization of impeller and housing geometry to reduce a wastewater pump's susceptibility to clogging, these measure cannot guarantee ultimate clog-free operation due to the heterogeneous nature of real wastewater. Therefore, another highly relevant field of research is the detection of clogging in wastewater pumps. There exist approaches leveraging the absolute discharge pressure and its frequency components as a proxy for the clogging state of a wastewater pump [29,30]. With such approaches, the response to imminent critical clogging can be adapted to an operator's needs. One exemplary action might be the triggering of a so-called cleaning sequence [8], enabled by the use of a VFD, which can help automate the removal of an acute clogging phenomenon. At the very least, an early warning system can be put in place to better manually respond to critical clogging scenarios.

Overall, this multifaceted overview of challenges and solutions in regards to the optimization potential of pressurized sewerage systems with a focus on wastewater pumping stations presents several in-depth methodological approaches and demonstrates their applicability and practical relevance. This encapsulates the transport of sediments from suction chambers through the wastewater pumps and quantifies their potential effects on the components involved. It highlights the nexus of functionality and achievable efficiency while maintaining feasibility for an optimized, modern perspective on pressurized sewerage systems as critical infrastructure.

Author Contributions: Conceptualization, T.R., T.N., D.B., F.B. and P.U.T.; methodology, T.R., T.N., D.B. and F.B.; software, T.R., T.N., D.B. and F.B.; validation, T.R., T.N., D.B. and F.B.; formal analysis, T.R., T.N., D.B. and F.B.; investigation, T.R., T.N., D.B. and F.B.; resources, P.U.T.; data curation, T.R., T.N., D.B. and F.B.; writing—original draft preparation, T.R. and F.B.; writing—review and editing, T.R., T.N., D.B., F.B. and P.U.T.; visualization, T.R., T.N., D.B. and F.B.; supervision, P.U.T.; project administration, P.U.T.; All authors have read and agreed to the published version of the manuscript.

Funding: This research study received no external funding.

Institutional Review Board Statement: Not applicable.

Informed Consent Statement: Not applicable.

Data Availability Statement: The datasets presented in this article are not readily available due to non-disclosure clauses.

Conflicts of Interest: The authors declare no conflicts of interest.

Nomenclature

Roman letters

A	area	[m^2]
$\hat{A}$	amplitude	[bar]
c	degree of coverage	[-]
CF	correction factor	[-]
d	depth	[mm]
D	diameter	[m]
F	force	[N]
Fr	Froude number	[-]
g	gravitational acceleration	[ms^{-2}]
h	height	[m]
H	head	[m]
L	characteristic length	[m]
M	scaling factor	[-]
N	number of samples	[-]
n_q	specific speed (metric)	[min^{-1}]
N_S	specific speed (US customary)	[min^{-1}]
p	particle size	[mm]
P	power	[W, kW]
Q	flow rate	[m^3s^{-1}, m^3h^{-1}, ls^{-1}]
R	radius	[mm]
Re	Reynolds number	[-]
s	gap width	[mm]
S	gap ratio	[-]
t	thickness	[mm]
T	time	[s]
u	relative position of leading edge	[-]
v	velocity	[ms^{-1}]
V	volume	[m^3]
$w(n)$	Hamming window function	[-]
We	Weber number	[-]

Greek letters

β	blade angle	[°]
η	efficiency	[-]
ν	kinematic viscosity	[m^2s^{-1}]
ρ	mass density	[kgm^{-3}]
σ	surface tension	[Nm^{-1}]
τ	torque	[Nm]
ϕ	wrap angle	[°]

Subscripts

A	average
ax	axial
BS	back shroud

c	critical
CW	clear water
HR	housing recess
el	electrical
H	hub
hydr	hydraulic
L	contamination class
M	model
max	maximum
MOD	modification
o	overall
O	original
p	peak
Pump	pump
r	radial
rms	root mean square
S	shroud
total	total
1	position of leading edge
2	position of trailing edge
Abbreviations	
BEP	best efficiency point
BPF	blade passing frequency
CFD	computational fluid dynamics
CW	clear water
DFT	discrete Fourier transform
DOE	design of experiments
FPT	long-time functional performance test
L	contamination class
LHS	Latin hypercube sampling
MOD	modification
NSGA	non-dominant sorting genetic algorithm
PC	polycarbonate
PLA	polylactide
PMMA	methyl methacrylate
PVC	polyvinyl chloride
RANS	Reynolds averaged Navier–Stokes
RF	rotational frequency
RMS	root mean square
RSO	response surface optimization
SST	Menter's shear stress transport turbulence model
VFD	variable-frequency drive

References

1. Crabtree, R.W. *A Classification of Combined Sewer Sediment Types and Characteristics*; Technical Report ER 324 E; WRc Engineering: Swindon, UK, 1988.
2. Kirchheim, N. *Kanalablagerungen in der Mischkanalisation*; Deutsche Vereinigung fuer Wasserwirtschaft, Abwasser und Abfall e. V. (DWA): Hennef, Germany, 2005.
3. Mitchell, R.L. Causes, Effects and Solutions of Operational Problems in Wastewater Systems Due to Nonwoven Wet Wipes. Ph.D. Thesis, Technische Universität Berlin, Berlin, Germany, 2019. [CrossRef]
4. Ackl, R.A. Enhancing the Design of the Wet Pit Pumping Stations Based on Experimental and Numerical Investigations. Ph.D. Thesis, Technische Universität Berlin, Berlin, Germany, 2018.
5. Deutsche Vereinigung für Wasserwirtschaft, Abwasser und Abfall e. V. (DWA). *Arbeitsblatt DWA-A 120-2: Pumpsysteme Außerhalb von Gebäuden—Teil 2: Pumpstationen und Drucksysteme*; DWA: Hennef, Germany, 2022.

6. ANSI/HI. *American National Standard for Rotodynamic Pumps for Pump Intake Design*; Technical Report ANSI/HI 9.8-2018; Hydraulic Institute: Parsippany, NJ, USA, 2013.
7. Surek, D. *Pumpen für Abwasser- und Kläranlagen—Auslegung und Praxisbeispiele*; Springer Vieweg: Wiesbaden, Germany, 2014. [CrossRef]
8. Gerlach, S.; Thamsen, P.U. Cleaning Sequence Counters Clogging: A Quantitative Assessment Under Real Operation Conditions of a Wastewater Pump. In Proceedings of the ASME 2017 Fluids Engineering Division Summer Meeting. American Society of Mechanical Engineers, Tampa, FL, USA, 2–8 November 2017; p. V01AT05A001. [CrossRef]
9. Gülich, J.F. *Centrifugal Pumps*; Springer: Cham, Switzerland, 2020. [CrossRef]
10. Ren, Y.; Zhao, L.; Mo, X.; Zheng, S.; Yang, Y. Visualization investigation of the motion of rags in a double blades pump. *AIP Adv.* **2024**, *14*, 015070. [CrossRef]
11. Pöhler, M. Experimentelle Entwicklung eines standardisierten Abnahmeverfahrens für Abwasserpumpen. Ph.D. Thesis, Technische Universität Berlin, Berlin, Germany, 2020.
12. Wesche, W. *Radiale Kreiselpumpen: Berechnung und Konstruktion der Hydrodynamischen Komponenten*; VDI-Buch, Springer Vieweg: Berlin, Germany, 2016. [CrossRef]
13. Schindl, H.; Payer, H.J. *Strömungsmaschinen. Band 1, Inkompressible Medien*; De Gruyter Oldenbourg: Munich, Germany; Vienna, Austria, 2015. [CrossRef]
14. Pöhler, M.; Thamsen, P.U. Mythos Kugeldurchgang—Aussage über Verstopfungsanfälligkeit bei Abwasserpumpen? *WWT Wasserwirtsch. Wassertech.* **2019**, *7*, 12–17. [CrossRef]
15. Beck, D.; Steffen, M.; Thamsen, P.U. How to Measure the Functionality of Sewage Pumps. In Proceedings of the 15th European Conference on Turbomachinery Fluid Dynamics & Thermodynamics, Budapest, Hungary, 24–28 April 2023. [CrossRef]
16. Beck, D.; Thamsen, P.U. Development of Sewage Pumps with Numerical and Experimental Support. *Int. J. Turbomach. Propuls. Power* **2023**, *8*, 18. [CrossRef]
17. Beck, D.; Thamsen, P.U. Optimization of a Closed 2-Channel Impeller with Experimental and Optical Support. In Proceedings of the ASME 2024 Fluids Engineering Division Summer Meeting, Anaheim, CA, USA, 15–17 July 2024. [CrossRef]
18. Nardone, R.; Flitney, B. The effect of impeller back pump-out vanes on seal performance. *Sealing Technol.* **2006**, *2006*, 9–11. [CrossRef]
19. Karassik, I.J.; McGuire, T. *Centrifugal Pumps*; Springer: New York, NY, USA, 1998. [CrossRef]
20. Schulz, H. *Die Pumpen*; Springer: Berlin/Heidelberg, Germany, 1977. [CrossRef]
21. Rinnert, T.; Thamsen, P.U. Experimental Investigation of the Influence of the Axial Gap Width in the Back Shroud Cavity on the Clogging Behavior of a Wastewater Pump. In Proceedings of the 16th European Turbomachinery Conference (ETC16), Garbsen/Hannover, Germany, 24–28 March 2025. [CrossRef]
22. Rinnert, T.; Thamsen, P.U. The Effect of Backward Curved Back Vanes and Back Channels on Fiber Entry Into the Back Shroud Cavity of a Wastewater Pump. *J. Fluids Eng.* **2026**, *148*, 081001. [CrossRef]
23. Nitzsche, T.; Peter, J.; Haueisen, S.; Thamsen, P.U. Design Recommendations for Wastewater Pumping Stations—Results from Model Tests. In Proceedings of the Conference on Modelling Fluid Flow (CMFF), Budapest, Hungary, 30 August–2 September 2022.
24. Beck, D.; Thamsen, P.U. Methodology for the Development of a Closed 2-Channel Impeller with low Susceptibility to Clogging. *J. Fluids Eng.* **2024**, *146*, 071102. [CrossRef]
25. Beck, D.; Thamsen, P.U. Improving Functionality of a High-Efficiency Semi-Open 2-Channel Impeller by Connected Leading Edges. In Proceedings of the ASME 2025 Fluids Engineering Division Summer Meeting, Philadelphia, PA, USA, 27–30 July 2025. [CrossRef]
26. Beck, D.; Brokhausen, F.; Thamsen, P.U. Time-Resolved Measurements for the Detection of Clogging Mechanisms. In Proceedings of the Fluids Engineering Division Summer Meeting. American Society of Mechanical Engineers, Toronto, ON, Canada, 3–5 August 2022.
27. Brokhausen, F.; Herfurth, E.; Beck, D.; Thamsen, P.U. Exploring Characteristics of Time-Resolved Signals in the Operation of Wastewater Pumps. In Proceedings of the 15th European Conference on Turbomachinery Fluid Dynamics & Thermodynamics, Budapest, Hungary, 24–28 April 2023. [CrossRef]
28. Beck, D.; Holzbauer, Y.; Thamsen, P.U. Different Clogging Behavior of Wastewater Pumps. In Proceedings of the Fluids Engineering Division Summer Meeting, Virtual, 10–12 August 2021. [CrossRef]
29. Brokhausen, F.; Rost, L.M.; Thamsen, P.U. Frequency Domain Analysis of Transient Discharge Pressure Harmonics for Clogging Detection in Wastewater Pumps. In Proceedings of the Fluids Engineering Division Summer Meeting, Anaheim, CA, USA, 15–17 July 2024. [CrossRef]
30. Brokhausen, F.; Thamsen, P.U. Leveraging Harmonic Distortion in Discharge Pressure for Clogging Detection in Wastewater Pumps. In Proceedings of the Fluids Engineering Division Summer Meeting, Philadelphia, PA, USA, 27–30 July 2025. [CrossRef]
31. Surek, D.; Stempin, S. *Technische Strömungsmechanik*; Springer Fachmedien: Wiesbaden, Germany, 2017. [CrossRef]
32. Strobl, T.; Zunic, F. *Wasserbau*; Springer: Berlin/Heidelberg, Germany, 2006. [CrossRef]
33. Heller, V. Scale Effects in Physical Hydraulic Engineering Models. *J. Hydraul. Res.* **2011**, *49*, 293–306. [CrossRef]

34. European Association of Pump Manufacturers (EUROPUMP). *Attainable Efficiencies of Volute Casing Pumps: A Reference Guide*; The Europump Guides to Advanced Pumping Technology, Guide No. 2; Elsevier Science Ltd.: Oxford, UK, 1999.
35. Versteeg, H.K.; Malalasekera, W. *An Introduction to Computational Fluid Dynamics*, 2nd ed.; Pearson Education Limited: Harlow, UK, 2007.
36. McKay, M.D.; Beckman, R.J.; Conover, W.J. A Comparison of Three Methods for Selecting Values of Input Variables in the Analysis of Output from a Computer Code. *Technometrics* **2000**, *42*, 55–61. [CrossRef]
37. Mitchell, R.L.; Gunkel, M.; Waschnewski, J.; Thamsen, P.U. Nonwoven Wet Wipes Can Be Hazardous Substances in Wastewater Systems—Evidences from a Field Measurement Campaign in Berlin, Germany. In Proceedings of the Frontiers in Water-Energy-Nexus—Nature-Based Solutions, Advanced Technologies and Best Practices for Environmental Sustainability, Salerno, Italy, 14–17 November 2018.
38. Brokhausen, F.; Thamsen, P.U. Exploring transient instationarities of mechanical load in the operation of wastewater pumps. In Proceedings of the Conference on Modelling Fluid Flow (CMFF), Budapest, Hungary, 26–29 August 2025. [CrossRef]
39. *ISO 9906:2012*(en); Rotodynamic Pumps—Hydraulic Performance Acceptance Tests—Grades 1, 2 and 3. Standard, International Organization for Standardization: Geneva, Switzerland, 2012.
40. Pfleiderer, C.; Petermann, H. *Strömungsmaschinen*; Springer: Berlin, Germany, 2005. [CrossRef]
41. Schultz-Grunow, F. Der Reibungswiderstand rotierender Scheiben in Gehäusen. *ZAMM—J. Appl. Math. Mech.* **1935**, *15*, 191–204. [CrossRef]
42. Ippen, A.T. The Influence of Viscosity on Centrifugal-Pump Performance. *J. Fluids Eng.* **2022**, *68*, 823–838. [CrossRef]
43. Daily, J.W.; Nece, R.E. Chamber Dimension Effects on Induced Flow and Frictional Resistance of Enclosed Rotating Disks. *J. Basic Eng.* **1960**, *82*, 217–230. [CrossRef]
44. Nece, R.E.; Daily, J.W. Roughness Effects on Frictional Resistance of Enclosed Rotating Disks. *J. Basic Eng.* **1960**, *82*, 553–560. [CrossRef]
45. Will, B.C.; Benra, F.K.; Dohmen, H.J. Investigation of the flow in the impeller side clearances of a centrifugal pump with volute casing. *J. Therm. Sci.* **2012**, *21*, 197–208. [CrossRef]
46. Bubelach, T. Untersuchung der Radseitenraumströmung in einer Einschaufelrad-Abwasserpumpe. Ph.D. Thesis, Technische Universität Berlin, Berlin, Germany, 2009.
47. Knop, M.; Baack, T.; Hohmeier, B.; Di Brino, M.; Petrak, G.; Kamps, M.; Dohmen, H.J.; Benra, F.K. Erfolgreicher Kampf gegen die Verzopfung—Entwicklung, Bau und erste Betriebserfahrungen eines optimierten Laufrads für Schmutzwasserpumpen. *Korresp. Abwasser Abfall* **2022**, *69*, 387–398. [CrossRef]
48. Lyons, R.G. *Understanding Digital Signal Processing*, 2nd ed.; Prentice Hall PTR: Upper Saddle River, NJ, USA, 2004.
49. Blackman, R.B.; Tukey, J.W. The measurement of power spectra from the point of view of communications engineering—Part I. *Bell Syst. Tech. J.* **1958**, *37*, 485–569. [CrossRef]
50. Brandt, A. *Noise and Vibration Analysis: Signal Analysis and Experimental Procedures*; John Wiley & Sons: Hoboken, NJ, USA, 2023. [CrossRef]

Disclaimer/Publisher's Note: The statements, opinions and data contained in all publications are solely those of the individual author(s) and contributor(s) and not of MDPI and/or the editor(s). MDPI and/or the editor(s) disclaim responsibility for any injury to people or property resulting from any ideas, methods, instructions or products referred to in the content.